Sofia University "St. Kliment Ohridski"
Faculty of Physics

Master's Thesis

Extraction of the Coulomb excitation yields of low-lying states of ^{214}Ra

Author:
Ivan ANASTASOV

Supervisor:
Prof. D. Sc. Georgi RAINOVSKI

Sofia, 2026

Contents

Motivation **2**

1 Theoretical approach **3**

1.1 Seniority scheme 3

1.2 Electromagnetic transition probabilities 6

1.3 Po-Rn-Ra isotonic chain at $N = 126$ 6

2 Experimental method **9**

2.1 Coulomb excitation 9

2.2 Two-body kinematics 11

3 Experimental setup **14**

3.1 ISOLDE 14

3.1.1 Production and post-acceleration of radioactive beam 15

3.2 Miniball spectrometer 17

4 Data analysis **22**

4.1 Timing 22

4.2 DSSSD calibration 24

4.3 HPGe calibration 29

4.4 Preliminary results 32

Summary and conclusions **37**

Bibliography **37**

Motivation

The nuclear shell model, combined with pairing correlations, provides a natural framework for describing the low-energy spectra of semi-magic nuclei. In configurations involving valence particles occupying a single high-j orbital, low-lying $J > 0$ states arise from the recoupling of unpaired nucleons and form multiplets characterized by the seniority quantum number ν. The generalized seniority scheme thus offers a simplified yet effective description of nuclear structure near closed shells [1].

The region around the neutron shell closure at $N = 126$ represents an important testing ground for this framework. In the even–even Po–Rn–Ra isotones, the low-lying yrast states are expected to be dominated by valence protons in the $\pi(1h_{9/2})$ orbital outside the doubly magic ^{208}Pb core. In this picture, the $B(E2; 2_1^+ \rightarrow 0_1^+)$ transition strength provides a direct measure of quadrupole collectivity and serves as a sensitive probe of seniority structure.

While shell-model calculations reproduce the excitation energies of the $N = 126$ isotones remarkably well, a significant discrepancy is observed for the $B(E2; 2_1^+ \rightarrow 0_1^+)$ value in ^{210}Po, where the calculated strength exceeds the experimental result by approximately a factor of two. It remains unclear whether this deviation is specific to ^{210}Po or reflects a more general limitation of the model near the shell closure. The absence of experimental $B(E2)$ data for ^{212}Rn and ^{214}Ra prevents a systematic assessment of this behavior.

To address this issue, a safe Coulomb-excitation experiment on ^{214}Ra was performed at HIE-ISOLDE. A post-accelerated ^{214}Ra beam was directed onto ^{120}Sn and ^{58}Ni targets, and the emitted γ rays were detected with the Miniball spectrometer [2]. The primary goal of the present work is to extract the $B(E2; 2_1^+ \rightarrow 0_1^+)$ transition strength and to determine whether the discrepancy observed in ^{210}Po persists with increasing proton number along the $N = 126$ isotonic chain.

With data taking completed, the current status of the analysis is presented. The final results will test whether the low-lying states of ^{214}Ra are consistent with a predominantly $\pi(1h_{9/2})^2$ configuration and will provide important constraints for shell-model descriptions in this region.

Chapter 1

Theoretical approach

1.1 Seniority scheme

To describe configurations of several valence nucleons outside a closed shell, it is useful to adopt a simplified theoretical framework. The seniority scheme provides such a description for configurations of the form j^n and offers clear insight into the structure of low-lying nuclear states. Due to pairing correlations, nucleons tend to form pairs coupled to total angular momentum $J = 0^+$. A fundamental question is therefore: what is the minimum number of particles required to generate a state with a given total spin J?

This minimum number is defined as the seniority quantum number ν. It represents the number of particles that remain unpaired with respect to $J = 0^+$ coupling, while the number of paired particles is given by $n-\nu$. A configuration with seniority $\nu+2$ may still produce the same total angular momentum J. This classification is particularly useful because many realistic nuclear interactions conserve the seniority quantum number [3].

Odd tensor interactions are known to preserve seniority. This can be demonstrated by considering a single-particle odd tensor operator acting on a j^2 configuration. In a two-particle system, only even values of J are allowed. Conservation of angular momentum therefore implies that an operator with odd multipolarity cannot connect states with $J = 0$. Consequently, matrix elements of the form

$$\langle j^2 J | O^k | j^2 J = 0 \rangle = 0 \tag{1.1}$$

vanish.

For a system with n particles, the corresponding operator may be written as a sum of single-particle operators,

$$U^k = \sum_{i=1}^{n} U_i^k. \tag{1.2}$$

Since odd tensor operators do not act on particles paired to $J = 0$, their contribution originates solely from unpaired particles. As a result, the dependence on the total number of particles n can be removed, yielding

$$\left\langle j^n \nu J' \left\| \sum_{i=1}^{n} U_i^k \right\| j^n \nu J \right\rangle = \left\langle j^\nu \nu J' \left\| \sum_{i=1}^{\nu} U_i^k \right\| j^\nu \nu J \right\rangle. \tag{1.3}$$

The seniority quantum number may also be affected by two-particle operators. Consider an odd tensor two-body interaction V_{ik}, which can be expressed as a sum of products

of single-particle operators. The corresponding matrix element in a j^n configuration with seniority ν is given by

$$\left\langle j^n \nu \alpha J \left| \sum_{i<k}^{n} V_{ik} \right| j^n \nu \alpha' J \right\rangle . \tag{1.4}$$

Here, α and α' denote additional quantum numbers. As in the single-particle case, interactions acting on nucleons paired to $J = 0$ cannot break the pairs. Their contribution is therefore diagonal and equal to

$$V_0 = \langle j^2 J = 0 | V_{ik} | j^2 J = 0 \rangle. \tag{1.5}$$

For even n, this contribution occurs $(n - \nu)/2$ times, leading to

$$\begin{aligned} \left\langle j^n \nu \alpha J \left| \sum_{i<k}^{n} V_{ik} \right| j^n \nu \alpha' J \right\rangle = \left\langle j^\nu \nu \alpha J \left| \sum_{i<k}^{\nu} V_{ik} \right| j^\nu \nu \alpha' J \right\rangle \\ + \frac{n-\nu}{2} V_0 \, \delta_{\alpha\alpha'}. \end{aligned} \tag{1.6}$$

These matrix elements depend linearly on the number of particle pairs coupled to $J = 0^+$ and reach their maximum near mid-shell. For attractive interactions, states with lower seniority lie lower in energy. In even-even nuclei, the ground state therefore corresponds to $\nu = 0$ with $J^\pi = 0^+$. In odd-mass nuclei, the ground state typically has $\nu = 1$ and $J = j$. This demonstrates that ground-state energies are largely determined by the number of paired nucleons.

From an experimental perspective, it is particularly informative to examine the energy difference between states with seniority $\nu = 0$ and $\nu = 2$. This difference is given by

$$\begin{aligned} E(j^n, \nu = 2, J) - E(j^n, \nu = 0, J = 0) &= \langle j^2 J | V | j^2 J \rangle + \frac{n-2}{2} V_0 - \frac{n}{2} V_0 \\ &= \langle j^2 J | V | j^2 J \rangle - V_0. \end{aligned} \tag{1.7}$$

Notably, this energy difference is independent of the number of valence particles n.

Even tensor operators do not preserve seniority and may connect states with $\Delta\nu = \pm 2$. Such operators play a central role in the calculation of electric quadrupole transition probabilities. For single-particle even tensor operators, the seniority scheme allows the reduction of matrix elements to configurations of j^ν, leading to

$$\begin{aligned} \left\langle j^n \nu \alpha J \left\| \sum_{i=1}^{n} U_i^k \right\| j^n (\nu - 2) \alpha' J' \right\rangle = \left[\frac{(n - \nu + 2)(2j + 3 - n - \nu)}{2(2j + 3 - 2\nu)} \right]^{1/2} \\ \times \left\langle j^\nu \nu \alpha J \left\| \sum_{i=1}^{\nu} U_i^k \right\| j^\nu (\nu - 2) \alpha' J' \right\rangle . \end{aligned} \tag{1.8}$$

For large values of j and n, the matrix elements depend on the fractional shell occupation $f = n/(2j + 1)$ and exhibit a characteristic $f(1 - f)$ behavior, with a maximum near mid-shell. This behavior is commonly encountered in the description of electric quadrupole transitions, whose reduced transition probability is given by

$$B(E2; J_i \to J_f) = \frac{1}{2J_i + 1} \left| \langle J_f \| Q \| J_i \rangle \right|^2 , \tag{1.9}$$

where Q denotes the electric quadrupole operator.

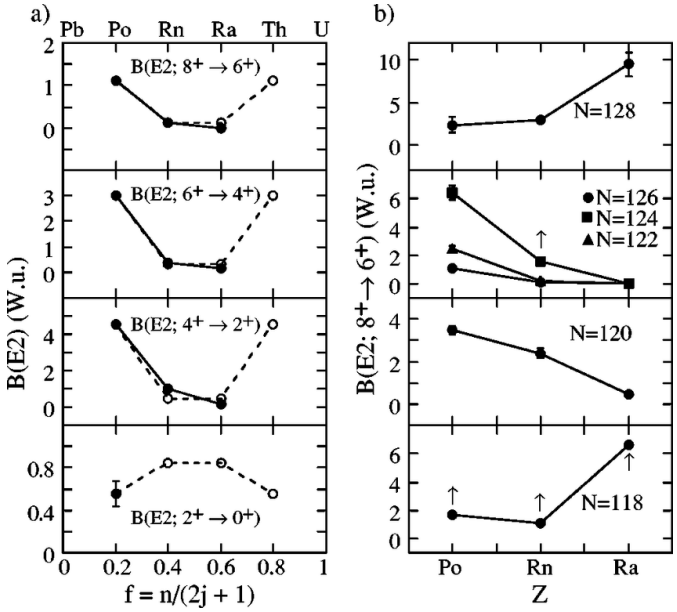

Figure 1.1: Experimental $B(E2)$ systematics for Po, Rn, and Ra isotones near the $N = 126$ shell closure. (a) $B(E2; 2_1^+ \to 0_1^+)$ values for semi-magic $N = 126$ isotones. (b) $B(E2; 8^+ \to 6^+)$ values for Po, Rn, and Ra isotones with $N = 118$–128. Figure taken from Ref. [6].

For partially filled shells with $(2j + 1) \gg n$, the transition probability is proportional to n^2, while it vanishes as n approaches $2j + 1$, corresponding to a closed shell. In the limit of large j and n, the general behavior can be expressed as

$$B(E2; 2^+ \to 0^+) \propto n\left(1 - \frac{n}{2j}\right) \approx f(1 - f). \tag{1.10}$$

For even tensor operators of higher rank that preserve seniority, a similar reduction applies:

$$\left\langle j^n \nu \alpha J \left\| \sum_{i=1}^{n} U_i^k \right\| j^n \nu \alpha' J' \right\rangle = \left(\frac{2j + 1 - 2n}{2j + 1 - 2\nu}\right) \left\langle j^\nu \nu \alpha J \left\| \sum_{i=1}^{\nu} U_i^k \right\| j^\nu \nu \alpha' J' \right\rangle. \tag{1.11}$$

In this case, the dependence on shell filling is governed by $(1 - 2f)$, indicating a change in sign of the matrix elements at mid-shell.

The most general case involves a two-particle even tensor interaction of rank $k > 0$, which may either conserve or change the seniority number. Such an interaction can be expressed as the product of two single-particle operators, one preserving seniority and one changing it. The corresponding matrix element takes the form

$$\left\langle j^n \nu \alpha J \left\| \sum_{i<k}^{n} V_{ik} \right\| j^n (\nu - 2) \alpha' J' \right\rangle = \left(\frac{2j + 1 - 2n}{2j + 1 - 2\nu}\right) \left[\frac{(n - \nu + 2)(2j + 3 - n - \nu)}{2(2j + 3 - 2\nu)}\right]^{1/2} \times \left\langle j^\nu \nu \alpha J \left\| \sum_{i<k}^{\nu} V_{ik} \right\| j^\nu (\nu - 2) \alpha' J' \right\rangle. \tag{1.12}$$

For $j, n \gg \nu$, the interaction energy varies as $(1-2f)f(1-f)$. It increases with increasing f, reaches a maximum near quarter filling, and crosses zero at mid-shell. Beyond mid-shell, the behavior is symmetric but with opposite sign.

1.2 Electromagnetic transition probabilities

The probability for electromagnetic decay of multipolarity $\sigma\lambda$, where σ specifies the type of transition (electric or magnetic) and λ its multipolarity, is given by

$$\Gamma(\sigma\lambda; I_1 \to I_2) = \frac{8\pi(\lambda+1)}{\lambda[(2\lambda+1)!!]^2}\left(\frac{E_\gamma}{\hbar c}\right)^{2\lambda+1} B(\sigma\lambda; I_1 \to I_2). \tag{1.13}$$

For magnetic dipole ($M1$) and electric quadrupole ($E2$) transitions, the decay widths can be written in practical units as

$$\Gamma(M1) = 11.57 \left[\frac{\text{meV}}{\mu_N^2}\right] E_\gamma^3 B(M1), \tag{1.14}$$

and

$$\Gamma(E2) = 8.06 \times 10^{-4} \left[\frac{\text{meV}}{e^2\,\text{fm}^4}\right] E_\gamma^5 B(E2). \tag{1.15}$$

Here E_γ denotes the transition energy in MeV, $B(E2)$ is expressed in $e^2\text{fm}^4$, $B(M1)$ in μ_N^2, and the decay width Γ is given in meV. The lifetime τ of an excited state is inversely proportional to the total decay width, such that $\tau = \hbar/\Gamma$. Consequently, electromagnetic transition probabilities can be extracted from lifetime measurements. Alternatively, the reduced transition probability $B(\lambda)$ may be determined directly from Coulomb excitation experiments.

In the case of mixed transitions, the multipole mixing ratio for a transition $I \to I-1$ is defined as

$$\delta\left(\frac{E2}{M1}\right) = 8.35 \times 10^{-3}\, E_\gamma \frac{\langle I-1\|E2\|I\rangle}{\langle I-1\|M1\|I\rangle}. \tag{1.16}$$

The reduced transition probability for an electromagnetic transition between states with spins I_1 and I_2 is given by

$$B(\sigma\lambda; I_1 \to I_2) = \sum_{\mu M_2} |\langle I_2 M_2|\sigma\lambda\mu|I_1 M_1\rangle|^2 = \frac{1}{2I_1+1}\,|\langle I_2\|\sigma\lambda\|I_1\rangle|^2\,. \tag{1.17}$$

1.3 Po-Rn-Ra isotonic chain at $N = 126$

The region around the neutron shell closure at $N = 126$ provides a testing ground for the validity of the seniority scheme close to magic numbers. In this mass region, low-energy excitations are expected to be dominated by valence protons occupying high-j orbitals, while the neutron core remains inert. As a result, seniority is anticipated to remain a good quantum number, leading to distinct and experimentally accessible signatures in excitation energies and electromagnetic transition strengths.

Within the nuclear shell model framework, the generalized seniority scheme offers a truncated yet effective description of such systems [1, 3]. For even–even nuclei, the lowest-lying yrast states are expected to follow a characteristic seniority-$\nu = 2$ pattern, where

excitation energies decrease with increasing angular momentum up to the maximum j^2 coupling, while the highest-spin state often manifests as an isomer. In addition, the absolute $E2$ transition strengths associated with seniority-changing transitions, $J^\pi = 2^+ \to 0^+$, are predicted to increase approximately parabolically with shell filling and to reach a maximum near mid-shell [1, 3]. Conversely, seniority-conserving transitions such as $J^\pi \to J^\pi - 2$ are expected to decrease towards mid-shell.

These features are observed in the even–even Po–Rn-Ra isotones with $N = 126$. The yrast structures of ^{210}Po, ^{212}Rn, and ^{214}Ra exhibit excitation-energy systematics consistent with seniority-$\nu = 2$ configurations dominated by the $\pi(1h_{9/2})^2$ proton configuration [4]. A graphical comparison between experimental level schemes and shell-model calculations is shown in Fig. 1.2, where the overall agreement supports the seniority interpretation for the yrast states.

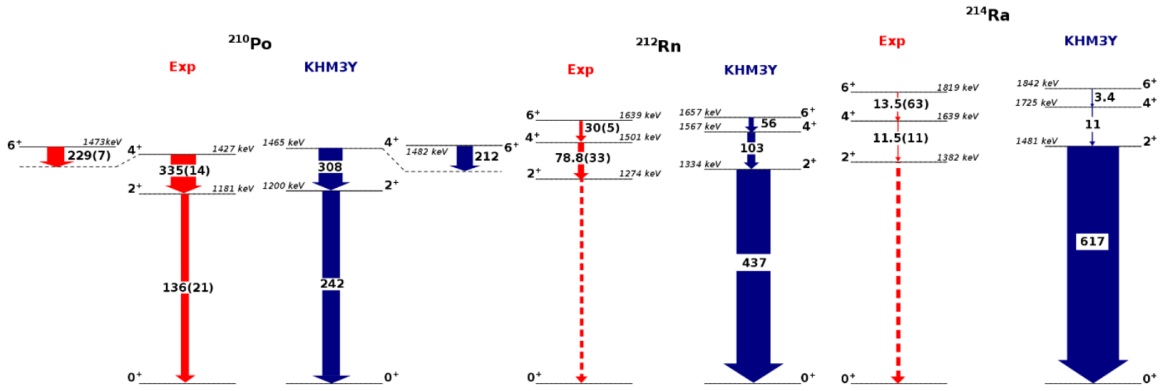

Figure 1.2: Comparison between experimental (Exp) and calculated (KHM3Y) properties of the yrast states in the $N = 126$ isotones ^{210}Po, ^{212}Rn, and ^{214}Ra. Energies are given in keV, and arrow thickness is proportional to the $B(E2)$ values (in $e^2\,\mathrm{fm}^4$) where available. Dashed arrows indicate transitions for which experimental $B(E2)$ values are not available. Figure adapted from Ref. [4].

While excitation energies and seniority-conserving transition strengths are in good agreement with shell-model predictions, the situation is less clear for the seniority-changing $E2$ transitions. For ^{210}Po, the calculated $B(E2; 2_1^+ \to 0_1^+)$ value exceeds the experimental result by approximately a factor of two [5, 4]. This discrepancy raises the question of whether quadrupole collectivity is systematically overestimated by the shell model near the $N = 126$ shell closure, or whether ^{210}Po represents a nucleus-specific deviation.

For ^{212}Rn and ^{214}Ra, experimental information on the $B(E2; 2_1^+ \to 0_1^+)$ transition is either scarce or entirely absent. As a consequence, the predicted parabolic increase of the $B(E2; 2_1^+ \to 0_1^+)$ strength along the Po–Rn–Ra chain at $N = 126$ cannot be tested experimentally. A systematic comparison between theory and experiment is therefore not yet possible.

This behavior is further illustrated in Fig. 1.3, which compares experimental (filled symbols) and calculated (open symbols) $B(E2)$ values for the $N = 126$ isotones. The absence of experimental data for ^{212}Rn and ^{214}Ra prevents a quantitative assessment of the seniority scheme for these nuclei and motivates new measurements in this region.

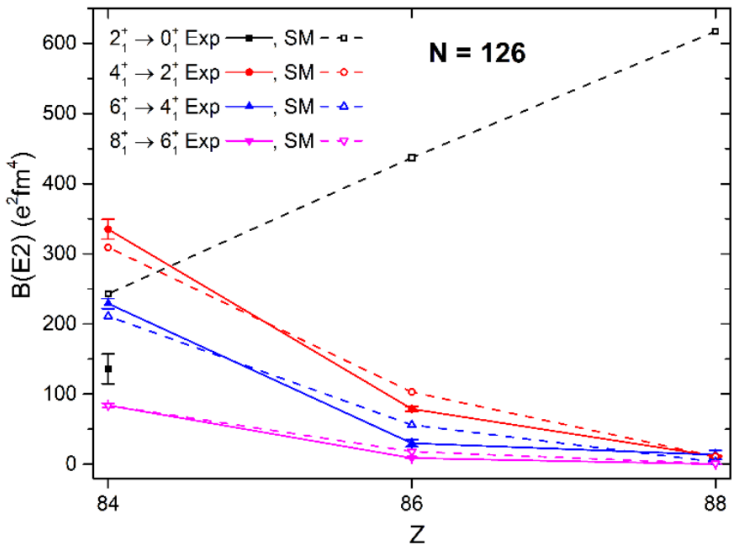

Figure 1.3: Comparison between experimental (filled symbols) and calculated (open symbols) $B(E2)$ strengths for the $N = 126$ isotones ^{210}Po, ^{212}Rn, and ^{214}Ra. Experimental data are taken from NNDC and the references therein. Figure adapted from Ref. [4].

The absence of experimental $B(E2; 2_1^+ \rightarrow 0_1^+)$ data for ^{212}Rn and ^{214}Ra represents a critical gap in the systematics of the $N = 126$ isotonic chain. Addressing this gap is one of the primary motivations of the present work, where safe Coulomb excitation is employed to measure electromagnetic transition strengths and to test whether the discrepancy observed in ^{210}Po persists with increasing proton number and to clarify the evolution of quadrupole collectivity above the $Z = 82$ shell closure.

Chapter 2

Experimental method

2.1 Coulomb excitation

Coulomb excitation[7], often referred to as electromagnetic excitation or Coulex, is a well-established method in nuclear structure studies. In this process, a nucleus is excited by the time-dependent electromagnetic field generated during an inelastic scattering interaction with another nucleus. The excitation mechanism is mediated by the exchange of virtual photons and, under appropriate conditions, can be described within a semi-classical framework.

The elastic scattering of heavy ions is described by the Rutherford cross section, which serves as the reference for Coulomb excitation processes:

$$\left(\frac{d\sigma}{d\Omega}\right)_{\text{Rutherford}} = \frac{1}{4}\frac{a^2}{\sin^2\left(\frac{\theta}{2}\right)}. \tag{2.1}$$

Here a denotes the half distance of closest approach and is given by

$$a = \frac{Z_p Z_t e^2}{m_0 v^2}, \tag{2.2}$$

where Z_p and Z_t are the atomic numbers of the projectile and target nuclei, m_0 is the reduced mass of the system, and v is the projectile velocity.

Within the semi-classical approximation, elastic scattering trajectories are treated classically. This approach is valid under conditions that can be characterized by dimensionless parameters. One such quantity is the Sommerfeld parameter η, which describes the effective strength of the Coulomb interaction:

$$\eta = 2\pi\frac{a}{\lambda} = \frac{Z_p Z_t e^2}{\hbar v}, \tag{2.3}$$

where λ is the de Broglie wavelength of the projectile.

When the energy transferred during the interaction is much smaller than the projectile energy, $\Delta E/E_p \ll 1$, the classical description of the trajectory remains valid. This condition is typically satisfied for heavy ions at relatively low kinetic energies. Under these circumstances, the Coulomb excitation cross section can be factorized into the Rutherford scattering cross section and the excitation probability:

$$\left(\frac{d\sigma}{d\Omega}\right) = P_n \left(\frac{d\sigma}{d\Omega}\right)_{\text{Rutherford}}. \tag{2.4}$$

The excitation probability of state n is expressed in terms of excitation amplitudes a_n as

$$P_n = \frac{1}{2J_i + 1} \sum_{m_i, m_n} |a_n|^2 , \tag{2.5}$$

where J_i denotes the angular momentum of the initial state, and m_i and m_n are the magnetic substates of the initial and final nuclear states, respectively.

To determine the excitation amplitudes, a perturbative treatment is employed in which the nuclear state $|\psi\rangle$ evolves according to the time-dependent Schrödinger equation

$$i\hbar \frac{\partial}{\partial t} |\psi\rangle = (H_0 + H_E(t)) \, |\psi\rangle, \tag{2.6}$$

where H_0 is the unperturbed nuclear Hamiltonian and $H_E(t)$ represents the time-dependent electromagnetic interaction.

The interaction Hamiltonian can be expressed using a multipole expansion as

$$H_E(t) = \sum_{\lambda\mu} \frac{4\pi Z_p e}{2\lambda + 1} \frac{1}{r_p^{\lambda+1}(t)} Y_{\lambda\mu}(\theta_p(t), \phi_p(t)) M^\dagger(E\lambda, \mu), \tag{2.7}$$

where $Y_{\lambda\mu}$ are spherical harmonics and $r_p(t)$, $\theta_p(t)$, and $\phi_p(t)$ describe the time-dependent position of the projectile nucleus.

The electric multipole operator is defined as

$$M(E\lambda, \mu) = \int d^3r \, r^\lambda Y_{\lambda\mu}(\theta, \phi) \rho(\mathbf{r}), \tag{2.8}$$

with $\rho(\mathbf{r})$ denoting the nuclear charge density.

The nuclear state can be written in the interaction picture as

$$|\psi\rangle = e^{-iH_0 t/\hbar} |\phi\rangle, \tag{2.9}$$

and the excitation amplitude is defined by

$$a_n(t) = \langle n|\phi\rangle. \tag{2.10}$$

Applying first-order perturbation theory, the time evolution of the excitation amplitudes is given by

$$i\hbar \dot{a}_n = \sum_m \langle n|H_E(t)|m\rangle e^{-i(E_m - E_n)t/\hbar}. \tag{2.11}$$

Assuming that excitation and de-excitation processes are infinitely separated in time, the boundary condition

$$a_n(t \to -\infty) = \delta_{0n} \tag{2.12}$$

is imposed. The excitation amplitude at $t \to +\infty$ then determines the Coulomb excitation probability.

For single-step excitations, the Coulomb excitation cross section for an electric transition of multipolarity λ can be written as

$$\sigma_{E\lambda} = \left(\frac{Z_p e}{\hbar v} \right)^2 a^{-2\lambda+2} B(E\lambda) f_{E\lambda}(E_x, E_{\text{beam}}, \lambda). \tag{2.13}$$

Similarly, the magnetic excitation cross section is given by

$$\sigma_{M\lambda} = \left(\frac{Z_p e}{\hbar c}\right)^2 a^{-2\lambda+2} B(M\lambda) f_{M\lambda}(E_x, E_{\text{beam}}, \lambda). \tag{2.14}$$

Here $B(E\lambda)$ and $B(M\lambda)$ denote the reduced transition probabilities, which are related to the multipole operators through

$$B(E\lambda; I_i \to I_f) = \frac{1}{2I_i + 1} \left|\langle I_f \| M(E\lambda) \| I_i \rangle\right|^2 . \tag{2.15}$$

To ensure that only electromagnetic interactions contribute to the excitation process, the distance of closest approach must satisfy the so-called safe Coulomb excitation condition[8],

$$a > \left[1.25\left(A_p^{1/3} + A_t^{1/3}\right) + 5\right] \text{ fm}. \tag{2.16}$$

As the multipolarity increases, Coulomb excitation cross sections decrease rapidly. In practice, low-lying collective states are predominantly excited through $E2$ transitions, while $E1$ transitions are typically suppressed. Coulomb excitation is therefore particularly well suited for selectively populating collective nuclear states. By measuring Coulomb excitation cross sections, reduced transition probabilities can be extracted and directly compared with shell-model predictions.

2.2 Two-body kinematics

In a two-body collision, a projectile transfers part of its kinetic energy to a target nucleus, leading to the excitation and recoil of the interacting nuclei. In order to properly interpret experimental observables such as scattering angles, recoil energies, and Doppler-shifted γ-ray energies, it is essential to analyze the kinematics of the reaction.

The interaction considered here can be described as a transformation from an initial *beam + target* system to a final *projectile + recoil* configuration. A projectile of mass m_B and initial kinetic energy E_B impinges on a target nucleus of mass m_T initially at rest. After the interaction, the scattered projectile carries energy E_p and momentum $\vec{p}_p$, while the recoiling target nucleus carries energy E_R and momentum $\vec{p}_R$. The two reaction products emerge at different angles with respect to the beam direction.

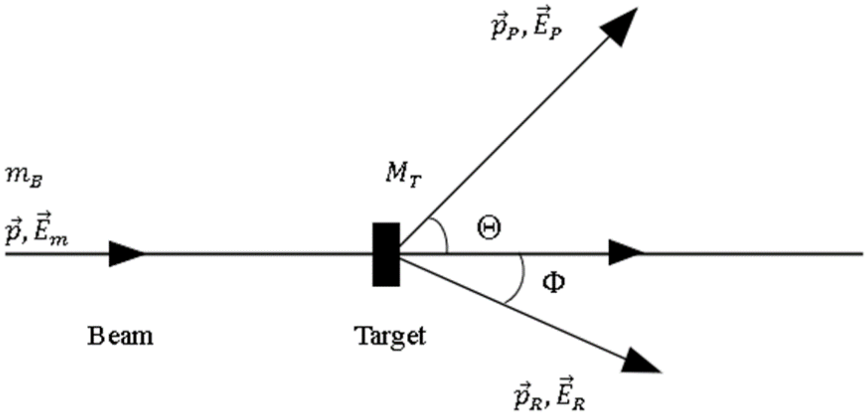

Figure 2.1: Kinematics of a two-body collision reaction in the laboratory frame.

In the present work, this formalism is applied to Coulomb excitation of a heavy projectile (^{214}Ra) on medium-mass targets (^{120}Sn and ^{58}Ni). For such inverse-kinematics conditions, the projectile is scattered predominantly at small laboratory angles, while the recoil nucleus is emitted at larger angles.

To derive the relevant relations, we consider momentum conservation and choose the beam direction to define the x-axis. The conservation of momentum then yields

$$p_B = p_p \cos\theta + p_R \cos\phi, \tag{2.17}$$
$$0 = p_p \sin\theta - p_R \sin\phi, \tag{2.18}$$

where θ and ϕ denote the scattering angles of the projectile and recoil, respectively.

Squaring Eqs. (2.17) and (2.18) and combining them leads to

$$p_R^2 = p_B^2 + p_p^2 - 2p_B p_p \cos\theta, \tag{2.19}$$
$$p_p^2 = p_B^2 + p_R^2 - 2p_B p_R \cos\phi. \tag{2.20}$$

Energy conservation can be expressed using the invariant mass of the system, which remains constant before and after the interaction:

$$p^2 = (E_B + m_T)^2 = (E_p + E_R)^2. \tag{2.21}$$

Using the relation $\vec{p}_B = \vec{p}_p + \vec{p}_R$, it follows that

$$E_B + m_T = E_p + E_R. \tag{2.22}$$

These expressions allow the projectile energy E_p to be written as a function of the scattering angle θ. Solving for the recoil energy and squaring both sides gives

$$E_R^2 = (E_B + m_T - E_p)^2. \tag{2.23}$$

Using the relativistic relation $E^2 = m^2 + p^2$ and substituting into the previous equations leads to a quadratic expression for the projectile momentum p_p:

$$\begin{aligned} p_P = {} & \frac{2p_B \cos\theta\,(E_B m_T + m_B^2)}{2\left[(E_B + m_T)^2 - p_B^2 \cos^2\theta\right]} \\ & \pm \frac{\sqrt{\left[2p_B \cos\theta\,(E_B m_T + m_B^2)\right]^2 - 4\left[(E_B + m_T)^2 - p_B^2 \cos^2\theta\right] p_B^2 (m_B^2 - m_T^2)}}{2\left[(E_B + m_T)^2 - p_B^2 \cos^2\theta\right]} \end{aligned} \tag{2.24}$$

Similarly, the recoil momentum p_R can be obtained by first expressing the projectile energy from energy conservation:

$$\left[(E_B + m_T)^2 - p^2 \cos^2\phi\right] p_R - 2p_B \cos\phi (E_B m_T + m_T^2) = 0, \tag{2.25}$$

which yields

$$p_R = \frac{2p_B \cos\phi (E_B m_T + m_T^2)}{(E_B + m_T)^2 - p_B^2 \cos^2\phi}. \tag{2.26}$$

The relationship between the scattering angles θ and ϕ can be derived by dividing Eqs. (2.19) and (2.20), resulting in

$$\tan\phi = \frac{\sin\theta}{\sqrt{E_B/E_p} - \cos\theta}, \tag{2.27}$$

where the previously established relationship between energy and momentum has been used.

In practice, the kinetic energy of the projectile at the interaction point differs from the nominal beam energy due to energy loss within the target material. This energy loss depends on the entrance energy and the depth at which the interaction occurs. For the present analysis, the effective interaction point is assumed to lie at half the target thickness, corresponding to an average energy loss $\overline{E}_{\mathrm{loss}}$, which is calculated using SRIM [9] simulations.

For Coulomb excitation in inverse kinematics, the heavy projectile is scattered at small angles, while the lighter target nucleus recoils at larger angles. This kinematic behavior is advantageous for experiments employing forward-angle particle detectors, allowing precise determination of scattering angles and energies. A detailed understanding of these relationships is essential for Doppler correction of γ-ray energies and for the extraction of reliable Coulomb excitation yields.

Chapter 3

Experimental setup

This section presents an overview of the laboratory and its current research activities. The primary objective is to study nuclear excited states produced through Coulomb excitation of accelerated radioactive beams. In addition, the experimental setup is described in detail to clarify the methodology employed.

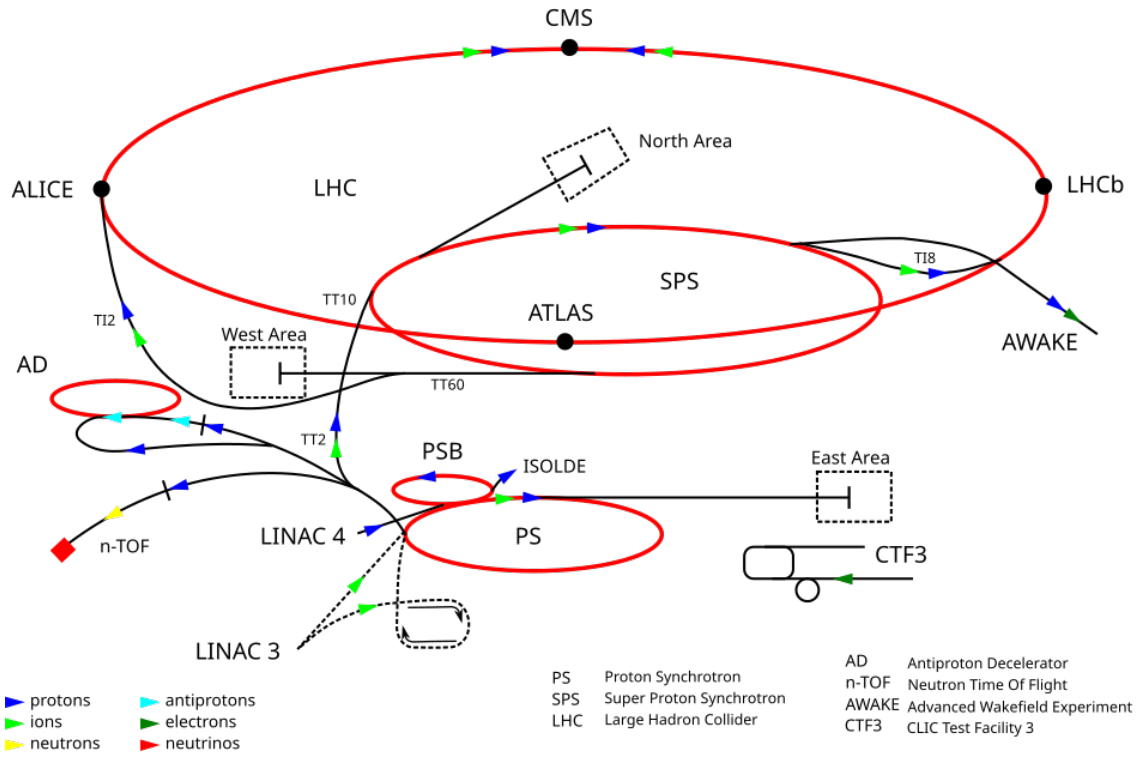

Figure 3.1: CERN Accelerator complex

3.1 ISOLDE

ISOLDE[10] traces its origins to 1967, when radioactive nuclei were first produced on line for experimental use in an initially provisional setup. Nearly five decades later, it remains the longest-running experiment at CERN, reflecting its sustained scientific relevance. ISOLDE has established itself as a leading facility in nuclear physics, having produced close to 1,300 isotopes spanning more than 70 chemical elements.

Over time, the facility has evolved into a center dedicated to both fundamental research and applied science. Its continued success rests on two main pillars. The first is the ongoing development of novel radioactive ion beams, accompanied by constant improvements in experimental performance and conditions. The second is the strength of the ISOLDE collaboration and research community, whose adaptability to an evolving scientific landscape has driven the creation of new concepts and instrumentation, ensuring a steady output of cutting-edge research. The figure shows a three-dimensional layout of the facility.

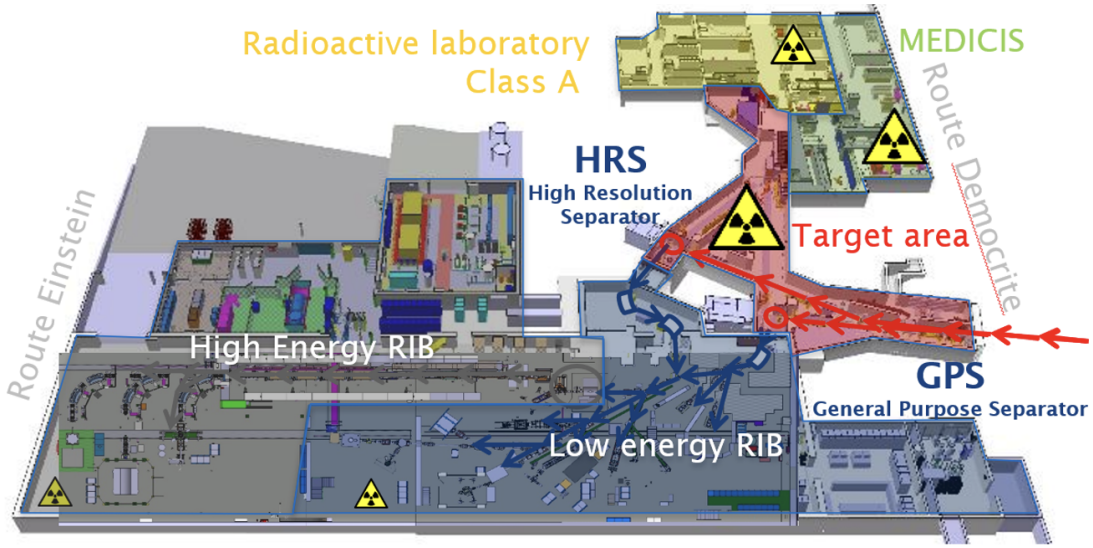

Figure 3.2: The layout of ISOLDE experimental hall

3.1.1 Production and post-acceleration of radioactive beam

Radioactive ion beams at ISOLDE are produced using high-energy proton-induced reactions. Protons delivered from the CERN Proton Synchrotron Booster (PSB), with a typical energy of 1.4 GeV and a maximum current of 2 μA, impinge on thick targets. Depending on experimental requirements, the proton energy can be reduced to approximately 1 GeV. A wide range of target materials is available at ISOLDE, with uranium carbide being among the most frequently used due to its properties.

During irradiation, nuclear reaction products are created inside the heated target material. To facilitate diffusion and effusion of the produced isotopes, the targets are operated at temperatures reaching up to 2000 °C. Once released from the target, the atoms are ionized in an adjacent ion source. Ionization can be achieved through several mechanisms, including surface ionization, plasma ionization, or laser ionization. By carefully matching the target material and ion-source type, high chemical selectivity can be obtained, enabling the production of more than one thousand isotopes across more than seventy chemical elements.

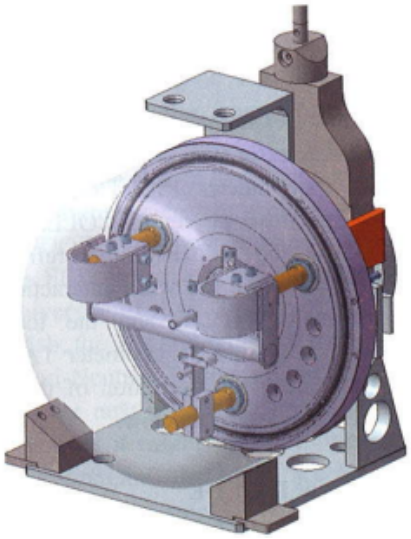

Figure 3.3: Schematic view of a standard ISOLDE target and ion source assembly used for the production of radioactive ion beams. High-energy protons impinge on a heated target material, where reaction products diffuse to the ion source and are selectively ionized prior to extraction.

For many experiments requiring high chemical purity, the Resonance Ionization Laser Ion Source (RILIS) [11] can be employed. This technique utilizes stepwise resonant photoionization, exploiting the unique atomic level structure of each element. Multiple laser beams are tuned to specific electronic transitions of the element of interest, ensuring that only the desired isotope is ionized. The ionization process takes place inside a heated metal cavity, typically operated at temperatures of around 2000 K. This environment provides stable confinement of the atomic vapor and efficient laser–atom interaction. Due to the short residence time of atoms in the cavity, on the order of 100 μs, high-repetition-rate laser systems are required. Combined with magnetic mass separation, this method allows for simultaneous selection in atomic number Z and mass number A, resulting in high isobaric purity of the extracted beam.

After ionization, the ions are accelerated to an energy of 30 keV and guided to the mass-separation stage. A magnetic separator selects the isotope of interest based on its mass-to-charge ratio. Two separator systems are available: the General Purpose Separator (GPS), featuring an H-type magnet with a bending radius of 1.5 m and a bending angle of 70°, and the High-Resolution Separator (HRS), which consists of two C-type magnets with bending radii of 1 m and bending angles of 90° and 60°, respectively. The HRS provides significantly improved mass resolution, albeit at the cost of reduced beam intensity.

Following mass separation, the beam is cooled and bunched using a Radio Frequency Quadrupole Cooler and Buncher (RFQCB). Cooling is achieved through collisions with a buffer gas, typically helium or argon, while electrostatic fields are used to bunch the ions. This process improves beam quality and prepares the ions for efficient charge breeding.

Charge breeding is performed using an Electron Beam Ion Source (EBIS)[12]. Inside the EBIS, ions are trapped by electrostatic potentials and confined radially by the strong magnetic field of a superconducting solenoid. A dense, monoenergetic electron beam ionizes the trapped ions through successive electron-impact collisions, increasing their charge state. The charge-breeding time determines the final charge-state distribution. Once the desired charge state is reached, the ions are extracted by lowering the trapping poten-

tial and subsequently passed through another mass separator to select the appropriate mass-to-charge ratio.

The charge-bred beam is then injected into the REX linear accelerator. Initial acceleration is provided by a radio-frequency quadrupole, raising the beam energy to approximately 0.3 MeV/u. Further acceleration is achieved using a sequence of interdigital H-type resonators, ultimately increasing the beam energy to about 3 MeV/u.

A major upgrade of the facility, known as HIE-ISOLDE[13], has significantly extended the experimental capabilities by introducing a superconducting post-accelerator. This upgrade enables acceleration of radioactive ion beams to energies of up to 10 MeV/u, greatly expanding the range of accessible nuclear-structure and nuclear astrophysics studies. In addition, developments in target technology, ion-source performance, and beam-cooling techniques are expected to further enhance beam intensities and purity in future experiments.

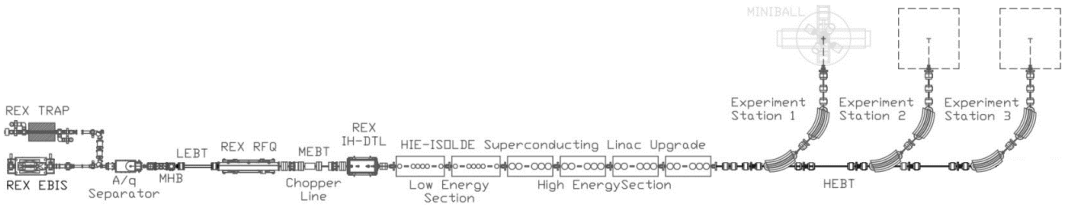

Figure 3.4: Layout of the ISOLDE post-acceleration infrastructure. After mass separation, the beam is cooled, charge-bred, and injected into the REX linear accelerator and the HIE-ISOLDE superconducting post-accelerator, enabling acceleration of radioactive ion beams to energies up to 10 MeV/u.

In this experiment, the radioactive beam was extracted in molecular form as ^{214}RaF in order to suppress isobaric contamination from surface-ionized francium. After mass separation, the molecular beam was accumulated and cooled in the REXTRAP Penning trap [14], where the molecular bond is dissociated. The resulting atomic ions were subsequently transferred to the EBIS charge breeder and post-accelerated by the HIE-ISOLDE linear accelerator, yielding a purified ^{214}Ra beam without a significant loss in overall efficiency.

3.2 Miniball spectrometer

The Miniball spectrometer [2] is a high-resolution γ-ray detection system based on segmented high-purity germanium (HPGe) detectors and has been in continuous operation at the ISOLDE facility at CERN for more than two decades. It was specifically designed for experiments involving low multiplicity reactions and low-intensity radioactive ion beams, making it particularly well suited for Coulomb excitation and transfer reaction studies.

The Miniball array consists of 24 encapsulated HPGe crystals arranged into eight detector clusters. Each cluster typically contains three tapered crystals, forming a compact geometry optimized for high detection efficiency and good angular resolution. The detector array is capable of operating with radioactive ion beams at energies up to approximately 5 MeV/u and has played a central role in a wide range of experiments at ISOLDE.

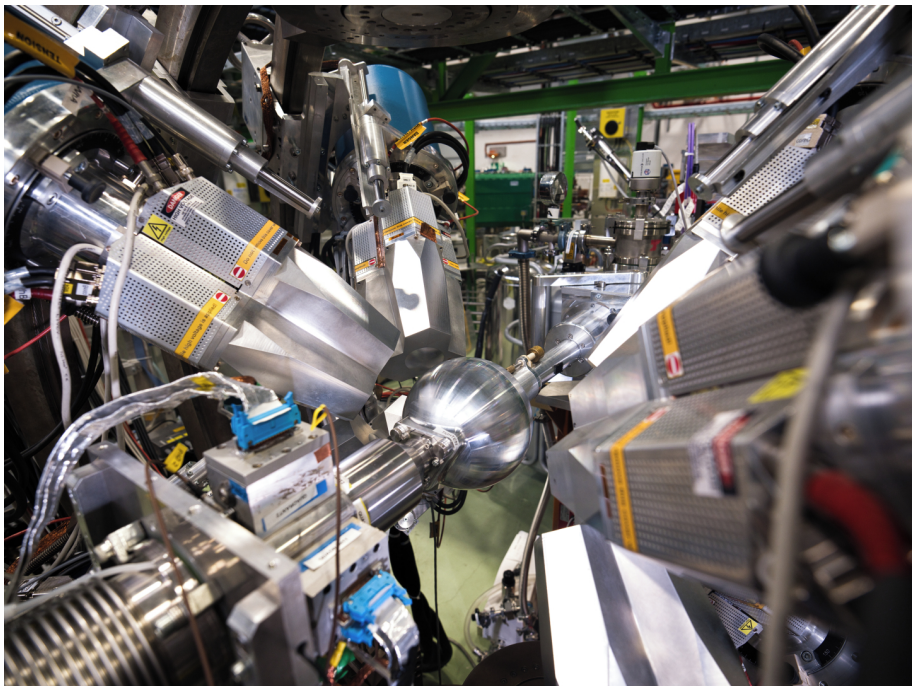

Figure 3.5: The Miniball spectrometer installed at ISOLDE. The detector clusters are arranged around the target position to provide high γ-ray detection efficiency and angular coverage.

Each Miniball crystal has a quasi-cylindrical geometry with a hexagonally tapered front face. The crystals are electrically segmented into six outer segments and a central core electrode. This segmentation enables precise determination of the γ-ray interaction position through pulse-shape analysis and segment multiplicity information.

The central core electrode is AC-coupled to its preamplifier and operated at high voltage, while the six outer segments are DC-coupled to individual preamplifiers. The cold electronics, including the field-effect transistors (FETs) and coupling capacitors, are mounted on the capsule lid in close proximity to the germanium crystal to minimize electronic noise. These components are thermally anchored to the cold finger of the cryostat.

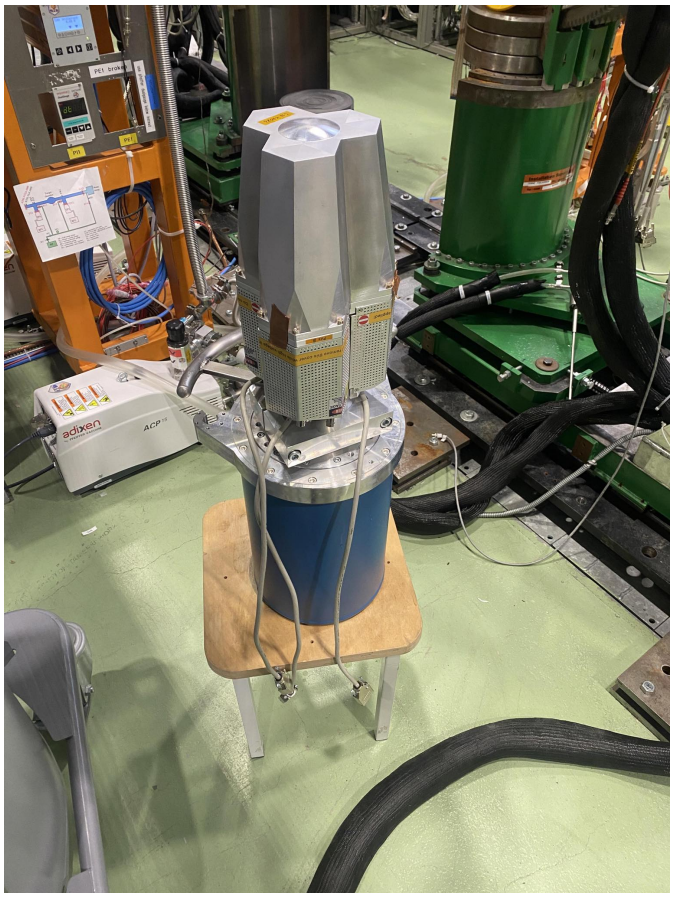

Figure 3.6: Dismounted Miniball HPGe detector crystal with the cooling system visible, showing the compact cryostat design and electrical feedthroughs.

The germanium crystals are housed in permanently sealed aluminum cryostats, allowing access to the cold electronics without the need for a clean-room environment. Each cryostat accommodates either three or four encapsulated crystals, depending on the configuration. In the present experimental setup, only triple-cluster configurations are employed.

Cooling of the crystals is achieved using liquid nitrogen supplied from a Dewar located behind the detector assembly. The cold finger maintains the operating temperature of the crystals, while a high-vacuum environment (typically of the order of 10^{-6} mbar) inside the cryostat ensures thermal insulation from the external environment. Temperature monitoring is performed using PT100 sensors mounted near the detector capsules.

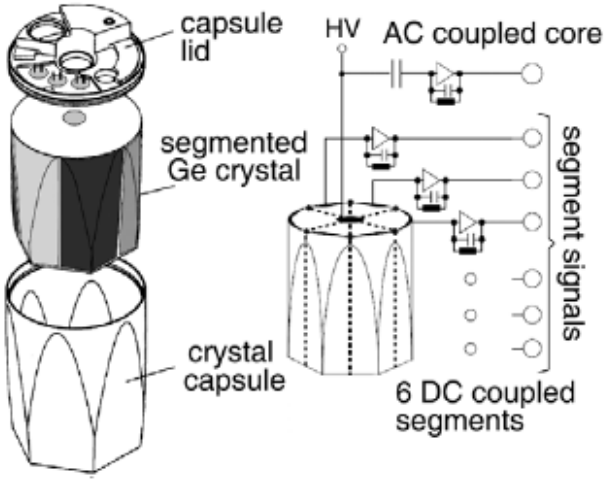

Figure 3.7: Schematic layout of the germanium crystal .

The accelerated radioactive beam is transported to the target chamber, which is located at the center of the Miniball array. The target chamber is a thin-walled, spherical vacuum vessel with an inner radius of approximately 80 mm, machined from a single block of $AlMg_3$. Inside the chamber, a target wheel is installed, capable of holding up to six different targets. This design allows rapid switching between targets during an experiment without breaking vacuum conditions.

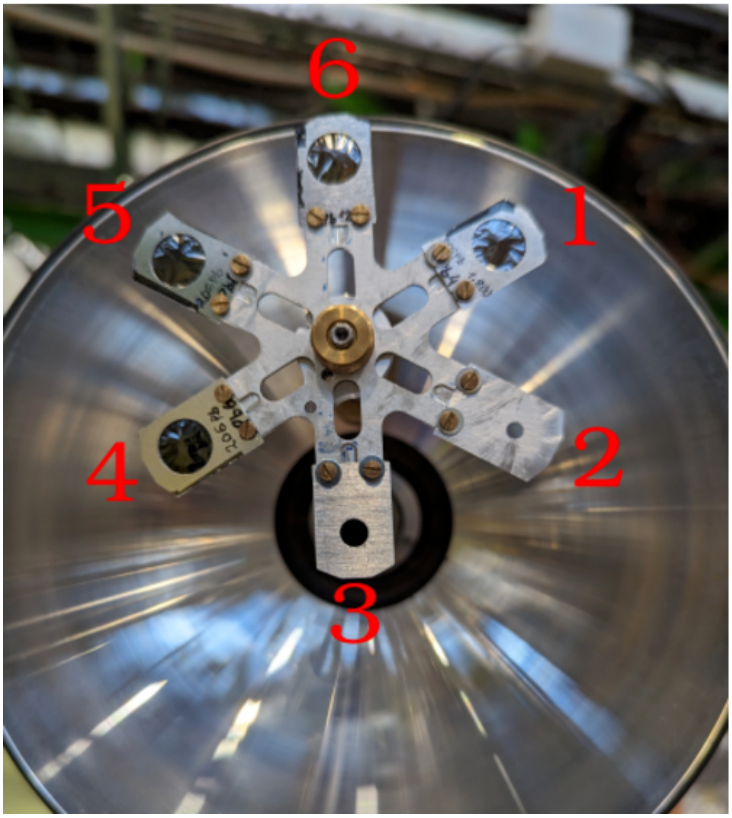

Figure 3.8: Miniball target wheel inside the target chamber.

Typically, two positions on the target wheel are reserved for beam-tuning frames with small and large apertures, while the remaining positions are dedicated to reaction targets.

The Miniball detector clusters are arranged approximately 10 cm from the target center, forming an almost spherical geometry around the reaction point. This configuration provides a solid-angle coverage of about 60% of 4π. The detectors are positioned at angles of approximately 45° in the forward direction and 135° in the backward direction with respect to the beam axis.

For particle detection in Coulomb excitation experiments, a Double-Sided Silicon Strip Detector (DSSSD) is mounted downstream of the target chamber, facing the beam direction. The DSSSD is typically positioned 25–31 mm from the target and is capable of detecting both beam-like and target-like particles scattered within its angular acceptance.

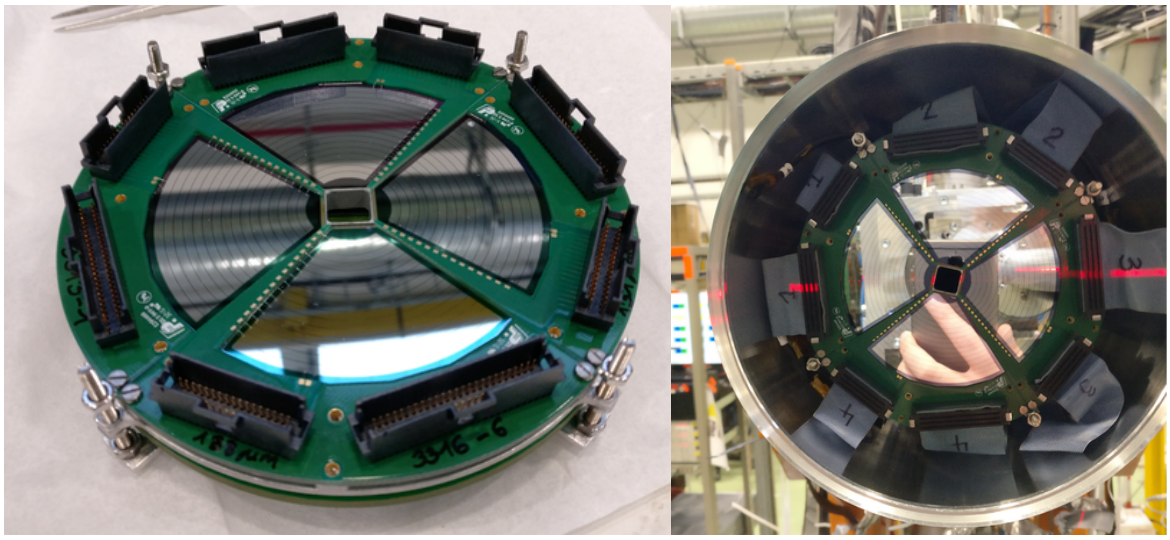

Figure 3.9: Double-sided silicon strip detector (DSSSD) in unmounted (left) and mounted (right) configurations.

Each DSSSD quadrant is segmented into 16 concentric rings on the front side, with a strip width of 1.9 mm and a 2.0 mm gap between adjacent rings. The smallest ring has an inner radius of 9 mm, resulting in angle coverage from approximately 20° to 60°. The back side of each quadrant is divided into 12 sectors, each spanning an angular width of 3.4°. Together, these segmentations provide precise angular resolution for particle identification and kinematic reconstruction.

The combined use of the Miniball γ-ray spectrometer and the DSSSD particle detector enables event-by-event Doppler correction of γ-ray energies and the extraction of reliable Coulomb excitation yields, forming the experimental basis for the present study.

Chapter 4

Data analysis

During the experiment, digital signal processing was performed using FEBEX modules to record signals from the Miniball HPGe detectors, the DSSSD particle detector, and the EBIS timing signal, with all data written to a common storage system for offline analysis. The data processing was carried out using the MiniballSort framework [18]. In the initial stage, the raw FEBEX data are converted into ROOT format and globally time-sorted. In the following step, calibrated events are constructed by applying detector-specific calibration parameters and imposing appropriate software thresholds. In the third stage, the reconstructed events are used to produce the observables, including timing correlations between detectors, particle energy spectra, and Doppler-corrected γ-ray spectra. These spectra are generated with particle coincidence conditions and form the basis for the extraction of Coulomb-excitation yields.

4.1 Timing

EBIS time gate

Since the radioactive beam is delivered in well-defined bunches extracted from the EBIS, the γ-ray time distribution is strongly correlated with the EBIS extraction signal. In the offline sorting, only γ rays within a fixed time window after the EBIS extraction were kept. A time gate of 1.2 ms was applied, corresponding to the period during which the extracted beam reaches the target and beam–target reactions are expected at the Miniball setup. This cut suppresses γ rays originating from β decay, long-lived activity, and other uncorrelated background sources, so that the remaining events are predominantly associated with the Coulomb-excitation reaction. After applying the EBIS time gate, less than 1% of the total γ-ray events remain.

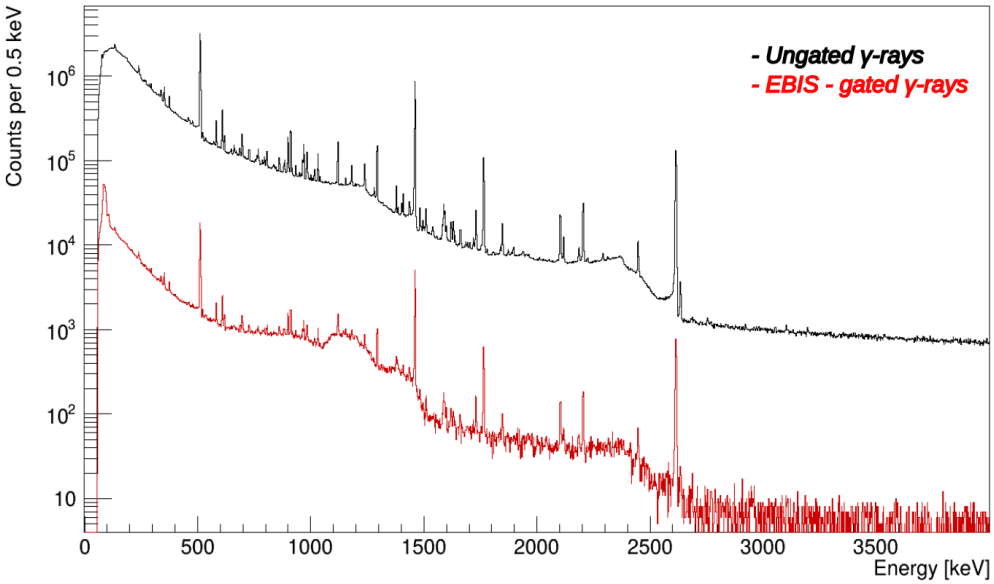

Figure 4.1: Combined γ-ray energy spectrum shown on a logarithmic scale. The black spectrum includes all detected γ-rays recorded during the experiment, while the red spectrum shows γ-rays retained after applying the EBIS time gate. The EBIS selection significantly reduces background contributions while preserving the γ-rays associated with beam–target reactions.

Particle–γ timing

The identification of true particle–γ coincidences between the DSSSD and the Miniball HPGe array is based on the time difference between particle and γ signals. A time-difference spectrum is constructed for particle–γ pairs.

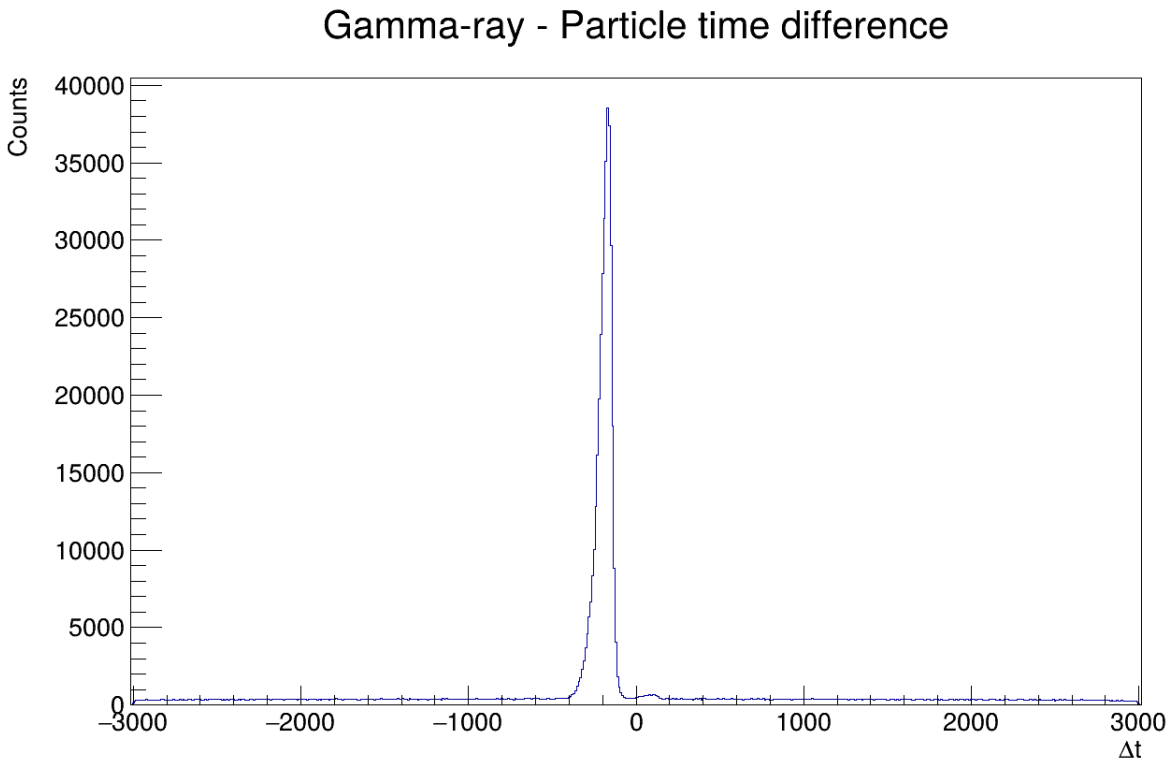

Figure 4.2: Particle–γ time-difference spectrum. The narrow peak corresponds to prompt coincidences, while the flat distribution arises from random coincidences.

A narrow peak is observed around zero time difference, corresponding to correlated particle–γ events from the Coulomb-excitation reaction. A prompt time window is defined around this peak and is used to select true coincidences associated with the de-excitation of the projectile-like and target-like nuclei.

The random contribution is estimated by applying an off-peak time gate in the particle–γ time-difference spectrum. The corresponding γ spectrum is normalized to the width of the prompt window and subtracted from the prompt-gated spectrum. This procedure yields particle-gated γ-ray spectra with significantly reduced background, which are subsequently used for Doppler correction and yield extraction.

4.2 DSSSD calibration

To reliably separate the ejectile (^{214}Ra) from the recoil (^{120}Sn) in the particle spectra and to enable accurate Doppler correction, a precise calibration of the DSSSD detector is required. This calibration is essential for optimizing the energy resolution of the Doppler-corrected γ-ray peaks, which is quantified by their full width at half maximum (FWHM). A minimized FWHM is the primary criterion for assessing the quality of the Doppler correction and directly impacts the precision with which γ-ray yields can be extracted. In the present experiment, this calibration step proved particularly time-consuming, as the detector had been operated extensively prior to the measurement and showed clear signs of radiation damage, indicating that it was approaching the end of its operational lifetime. Consequently, dedicated calibration procedures were necessary to recover a stable and

well-resolved response suitable for reliable yield determination with minimal systematic uncertainty.

Energy gain shift in the DSSSD detector

The first calibration issue identified was a gain shift affecting several channels of the DSSSD detector, visible directly in the raw energy spectra. Figure 4.3 shows the raw FEBEX spectra for one representative ring (SFP 1, board 0, channel 15), overlaid for three different groups of runs: runs 6–16, runs 29–41, and runs 42–55.

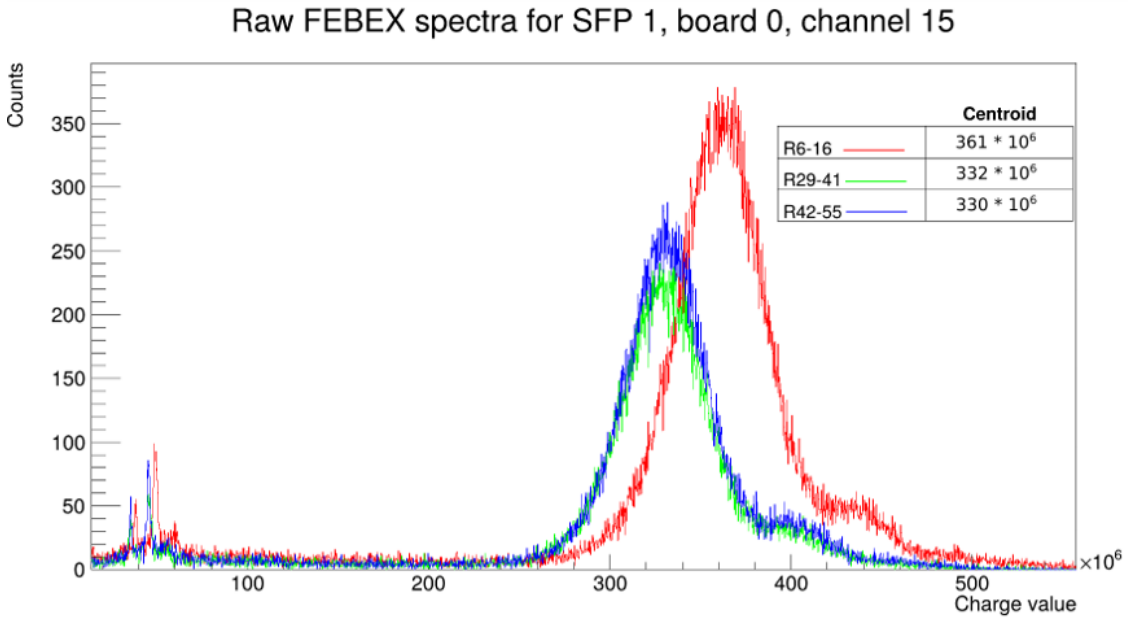

Figure 4.3: Raw FEBEX energy spectra for a representative DSSSD detector channel (SFP 1, board 0, channel 15), shown for three groups of runs: runs 6–16 (red), runs 29–41 (green), and runs 42–55 (blue). After runs 6–16, the peak position shifts toward lower channel numbers, indicating a change in the detector gain.

The spectrum corresponding to runs 6–16 exhibits a peak position at higher channel numbers, while the spectra from later runs are shifted toward lower channel numbers. This behavior indicates a reduction of the effective detector gain occurring after the initial phase of the experiment. The effect was most pronounced for the innermost strip, although smaller shifts were also observed in several other channels. In contrast, the spectra corresponding to runs 29–41 and 42–55 are mutually consistent, demonstrating a stable detector response once the gain change had occurred.

The observed gain variation is attributed to the high beam intensity at the beginning of the experiment combined with the aged condition of the detector, which had been used extensively in previous measurements. To properly account for this behavior, two independent energy calibrations were performed: one calibration for the initial runs (runs 6–16) and a second calibration applied to the remaining data set. This approach ensured a consistent energy response across the full data set and avoided systematic distortions in the subsequent analysis.

Comparison with kinematic simulations

To support the interpretation of the particle spectra and to guide the calibration procedure, kinematic simulations were performed for the ^{214}Ra + ^{120}Sn system. The particle energies were calculated using the KINSIM code [15], which is specifically designed for Coulomb-excitation experiments employing double-sided silicon strip detectors. In addition to two-body reaction kinematics, the code accounts for energy loss in the target material, energy losses in the dead layers of the DSSSD detector, and the full geometry of the experimental setup.

Figure 4.4 compares the simulated kinematic distribution with raw FEBEX spectra from a representative DSSSD detector channel. The simulation correctly reproduces the qualitative structure of the experimental spectrum, namely the presence of two distinct components corresponding to the ejectile (^{214}Ra) and the recoil (^{120}Sn). However, a clear quantitative discrepancy is observed in the separation between the two components, with the ratio of the peak separations reduced from $a/b \approx 2.05$ in the simulation to $a/b \approx 1.18$ in the experimental data.

This reduction in peak separation is attributed primarily to the charge deficit effect in the silicon detector [16]. For heavy ions at low energies, a fraction of the deposited energy is not converted into measurable charge due to enhanced recombination of electron–hole pairs along the dense ionization tracks. As a consequence, the detected pulse height underestimates the true deposited energy, with the magnitude of the effect depending on the ion species, energy, and stopping power. Since the projectile-like and target-like particles have different masses and velocities, the charge deficit affects them differently, leading to a compression of the experimentally observed kinematic separation compared to the ideal simulation.

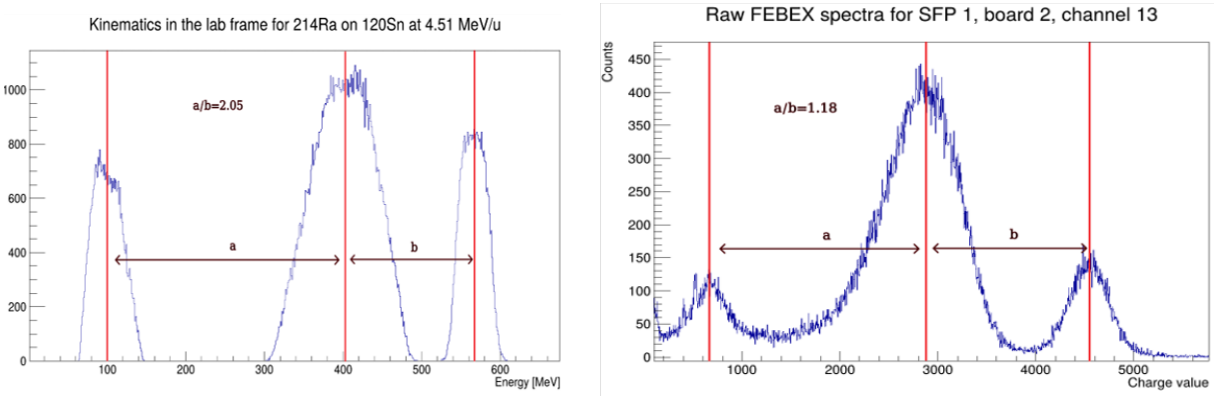

Figure 4.4: Comparison between simulated kinematic distributions and experimental raw FEBEX spectra for the ^{214}Ra + ^{120}Sn system. Left: simulated kinematics. Right: raw FEBEX spectrum for a representative DSSSD channel. While the simulation reproduces the qualitative structure, a reduced separation between projectile-like and target-like components is observed in the experimental data.

Despite this discrepancy, the simulation was used as a reference for the energy calibration of the DSSSD detector. In principle, the presence of multiple kinematically distinct features would allow for a multi-point calibration. In practice, however, the charge deficit distorts the relative peak positions, rendering a calibration based on multiple reference points unreliable. Instead, a single well-defined reference point was selected for the initial calibration, providing a stable and reproducible energy scale for subsequent analysis.

p-n correlation calibration method

The gain instabilities observed in the DSSSD detector, together with the non-uniform response of several channels, made it necessary to apply an alternative calibration strategy. For this reason, an independent calibration was performed for each data set using the p–n correlation method [17], which exploits the intrinsic coincidence between signals recorded on the front (p-side) and back (n-side) of the double-sided silicon strip detector.

As a reference for the calibration, p-side strip 13 was selected, corresponding to a angle range between 28° and 31°. Using this reference strip, energy–energy correlation histograms were constructed by selecting events with a multiplicity of exactly one particle hit, producing coincident signals in the reference p-strip and in a single n-strip. For each quadrant of the detector, this procedure was repeated for all n-side strips, with the calibrated p-strip energy plotted on one axis and the corresponding uncalibrated n-strip signal, expressed in ADC channels, plotted on the other.

The resulting correlations exhibited a linear dependence and were fitted with straight-line functions, allowing the gain and offset parameters of each n-strip to be extracted independently for all quadrants. Once the calibration of the n-side strips was completed, the procedure was inverted. In this second step, n-side strip 9 was chosen as the reference strip in each quadrant, and similar one-to-one coincidence conditions were applied between this calibrated n-strip and all p-side strips.

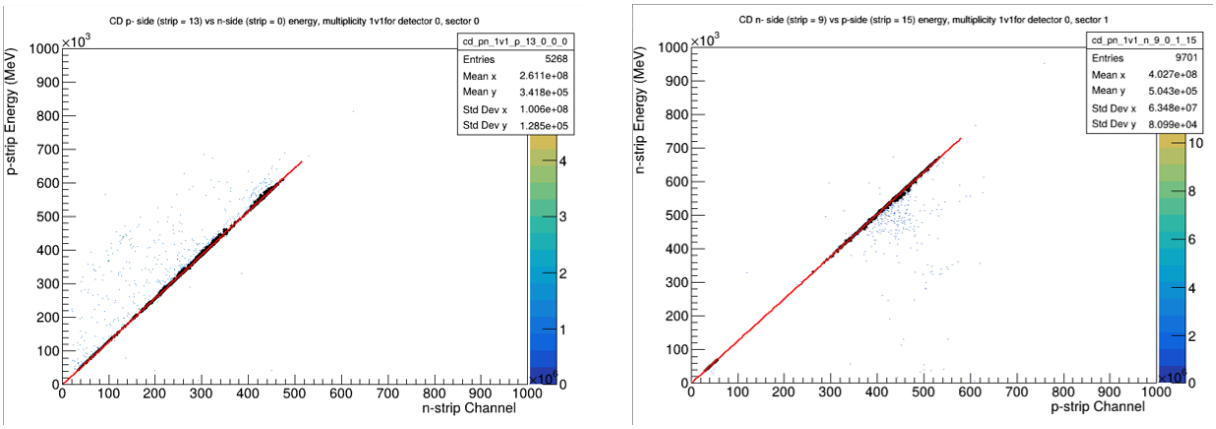

Figure 4.5: Two-step p–n cross-calibration procedure for the DSSSD. Left: calibration of n-side strips using p-side strip 13 as reference. Right: calibration of p-side strips using n-side strip 9 as reference. Linear correlations are used to extract gain and offset parameters for all strips.

Representative examples of the two calibration steps are shown in Fig. 4.5. The left panel illustrates the calibration of n-side strips using the reference p-strip, while the right panel shows the subsequent calibration of p-side strips using the calibrated n-side reference. In both cases, the clear linear correlations confirm the validity of the method and the good charge-sharing behavior of the detector.

Linear fits to these correlations were then used to determine the calibration parameters for the remaining p-side channels. This iterative p-n calibration procedure ensures a consistent energy response across both sides of the detector and effectively compensates for channel-dependent gain variations.

Fine-tuning of the DSSSD detector

After applying the kinematic simulation constraints and the p-n correlation calibration method, a final fine-tuning step was performed to further optimize the calibration of the DSSSD detector. This procedure aimed to reduce quadrant-to-quadrant differences that can affect the quality of the Doppler correction.

For this purpose, the four quadrants of the detector were treated independently and sorted separately. For each quadrant, the energy resolution was evaluated from the FWHM of the Doppler-corrected $2_1^+ \rightarrow 0_1^+$ transition γ-ray peak in ^{214}Ra. The quadrant exhibiting the best overall energy resolution, identified as quadrant Q1, was selected as a reference.

The calibration parameters of the remaining three quadrants were subsequently adjusted relative to this reference in order to minimize residual differences in the reconstructed particle energies. This fine-tuning procedure resulted in a small but systematic improvement of the γ-ray energy resolution and led to a more uniform detector response across all quadrants.

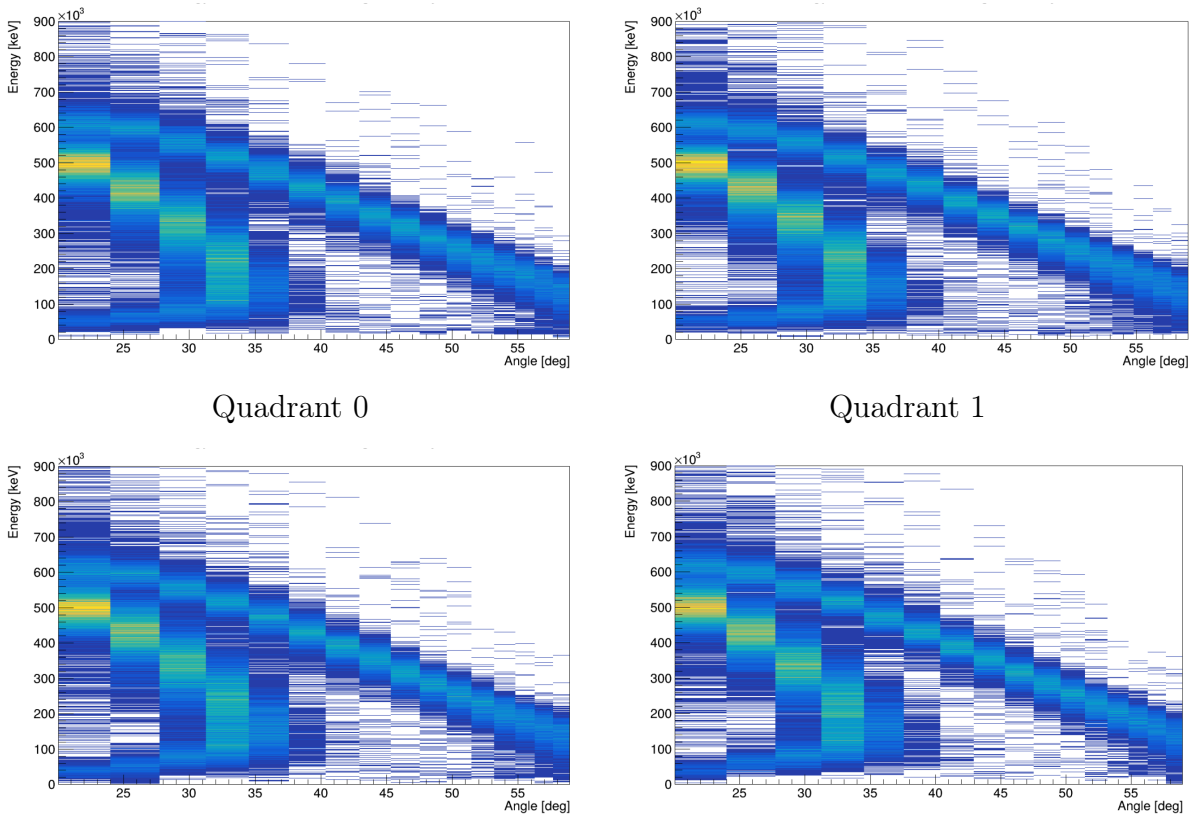

Figure 4.6: Particle energy in coincidence with a γ-ray for the four detector quadrants. The spectra are shown after the full calibration procedure and are used to compare the energy resolution across the detector.

The DSSSD energy calibration for the ^{58}Ni target was performed using the same procedure as for the ^{120}Sn data. In this case, the calibration was considerably simpler, since the particle energy spectra show only a single kinematic line associated with the target.

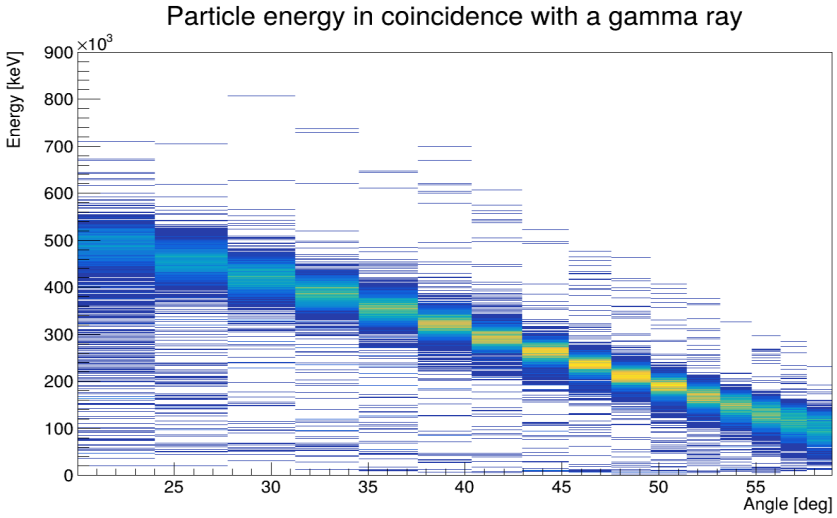

Figure 4.7: DSSSD particle energy spectrum obtained for the ^{58}Ni target after calibration.

The absence of a visible ^{214}Ra component in the particle spectra for the ^{58}Ni target is explained by reaction kinematics. Owing to the lower target mass, the scattered ^{214}Ra ions are confined to very small laboratory angles and predominantly pass through the central hole of the DSSSD, below the angular acceptance of about 20°.

4.3 HPGe calibration

Efficiency calibration

To correct measured γ-ray intensities, the relative efficiency of the Miniball HPGe array was determined from source runs with ^{152}Eu and ^{133}Ba placed at the target position. The spectra were summed over the array and the peaks were fitted with Gaussian functions using the nuclear spectroscopy analysis software HDTV [19]. For each transition, the relative efficiency point was obtained from the measured peak area normalized by the tabulated γ-ray intensity. The γ-ray energies, extracted yields, and relative statistical uncertainties used for the efficiency calibration are summarized in Table 4.1.

Table 4.1: Calibration lines used for the efficiency determination from ^{152}Eu and ^{133}Ba.

^{152}Eu calibration lines

E_γ (keV)	Yield	Error (%)
121.78	1.87×10^6	0.85
244.69	3.97×10^5	0.20
344.28	1.32×10^6	0.91
367.79	3.29×10^4	1.22
411.12	8.00×10^4	0.50
443.98	1.11×10^5	0.45
778.90	3.14×10^5	1.91
964.13	3.14×10^5	1.91
1112.12	2.63×10^4	2.47
1299.12	2.83×10^4	2.76
1408.01	3.51×10^5	1.71

^{133}Ba calibration lines

E_γ (keV)	Yield	Error (%)
80.99	4.94×10^6	0.16
223.12	6.22×10^5	0.43
276.40	9.92×10^5	0.40
302.85	2.39×10^6	0.21
356.01	6.76×10^6	0.15
383.86	1.02×10^6	0.32

The two source datasets were combined by scaling the ^{133}Ba efficiencies to the ^{152}Eu scale using an overlap-based normalization factor, and the merged set was then fitted with the same functional form as implemented in the Python analysis script:

$$\varepsilon(E) = \left(aE + \frac{b}{E}\right) \exp\left(cE + \frac{d}{E}\right), \tag{4.1}$$

where E is given in keV. The fit parameter uncertainties were obtained from the covariance matrix of the weighted least-squares fit.

Table 4.2: Fit parameters of the Miniball relative efficiency curve (Eq. 4.1).

Parameter	Value	Error (%)
a	5.903×10^{-4}	110
b	7.071×10^{2}	3.26
c	-6.797×10^{-4}	77
d	-1.316×10^{2}	1.66

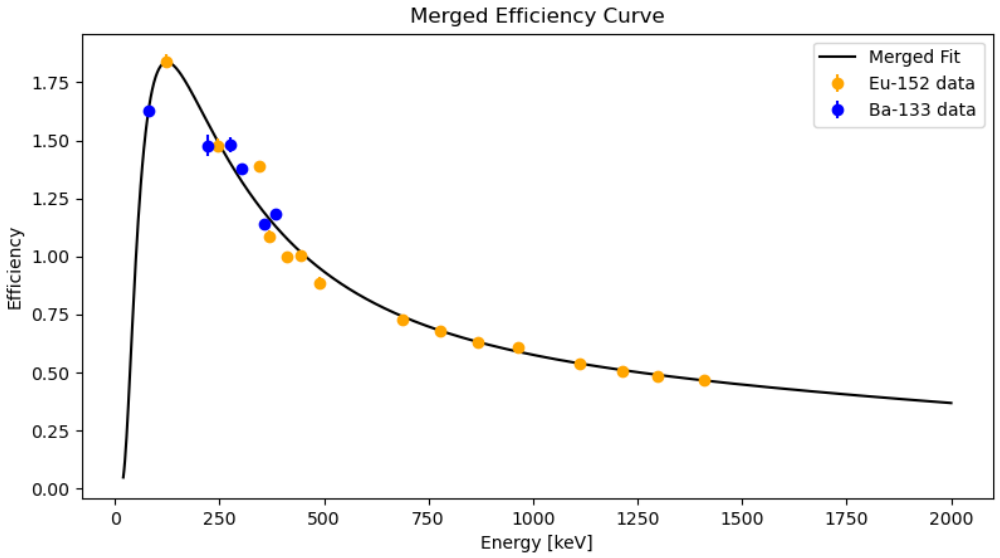

Figure 4.8: Relative efficiency of the Miniball HPGe array as a function of γ-ray energy. The points correspond to calibration data from ^{152}Eu and ^{133}Ba source measurements, while the solid curve represents the fitted efficiency function given in Eq. 4.1.

The resulting efficiency function was used to correct the experimental γ-ray yields.

Energy calibration

The energy calibration of the Miniball HPGe detectors was performed individually for each detector segment. Calibration runs with the same ^{152}Eu and ^{133}Ba sources used for the efficiency determination were analyzed. For each segment, well-resolved γ-ray peaks were fitted with Gaussian functions using HDTV, and the channel positions were extracted.

The relation between channel number and γ-ray energy was found to be linear over the investigated energy range. A linear function of the form

$$E = a + b \cdot C, \tag{4.2}$$

where C denotes the channel number, was therefore fitted to the calibration points of each segment separately. The fit parameters were obtained from a weighted least-squares procedure.

An example of the calibration for one detector segment is shown in Fig. 4.9.

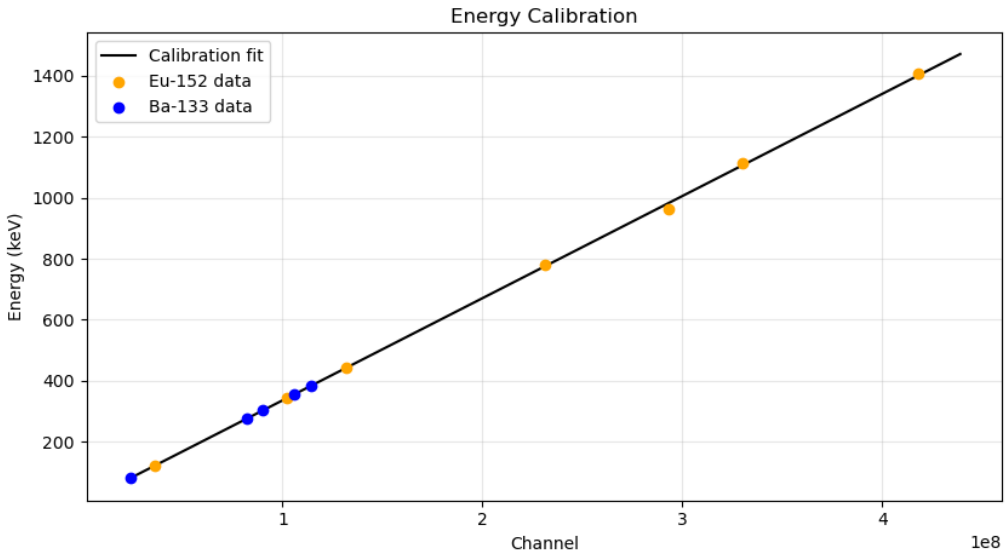

Figure 4.9: Example of the energy calibration for a single HPGe segment.

4.4 Preliminary results

Levels populated in this experiment

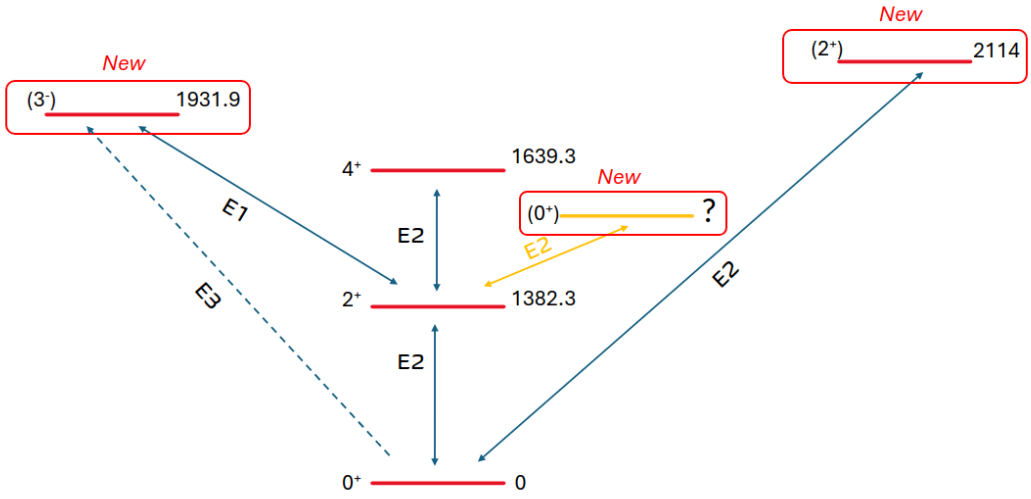

Figure 4.10: Level scheme of ^{214}Ra showing the states populated in the present Coulomb-excitation experiment. Newly observed states are highlighted. The arrows denote observed γ-ray transitions, with their multipolarities.

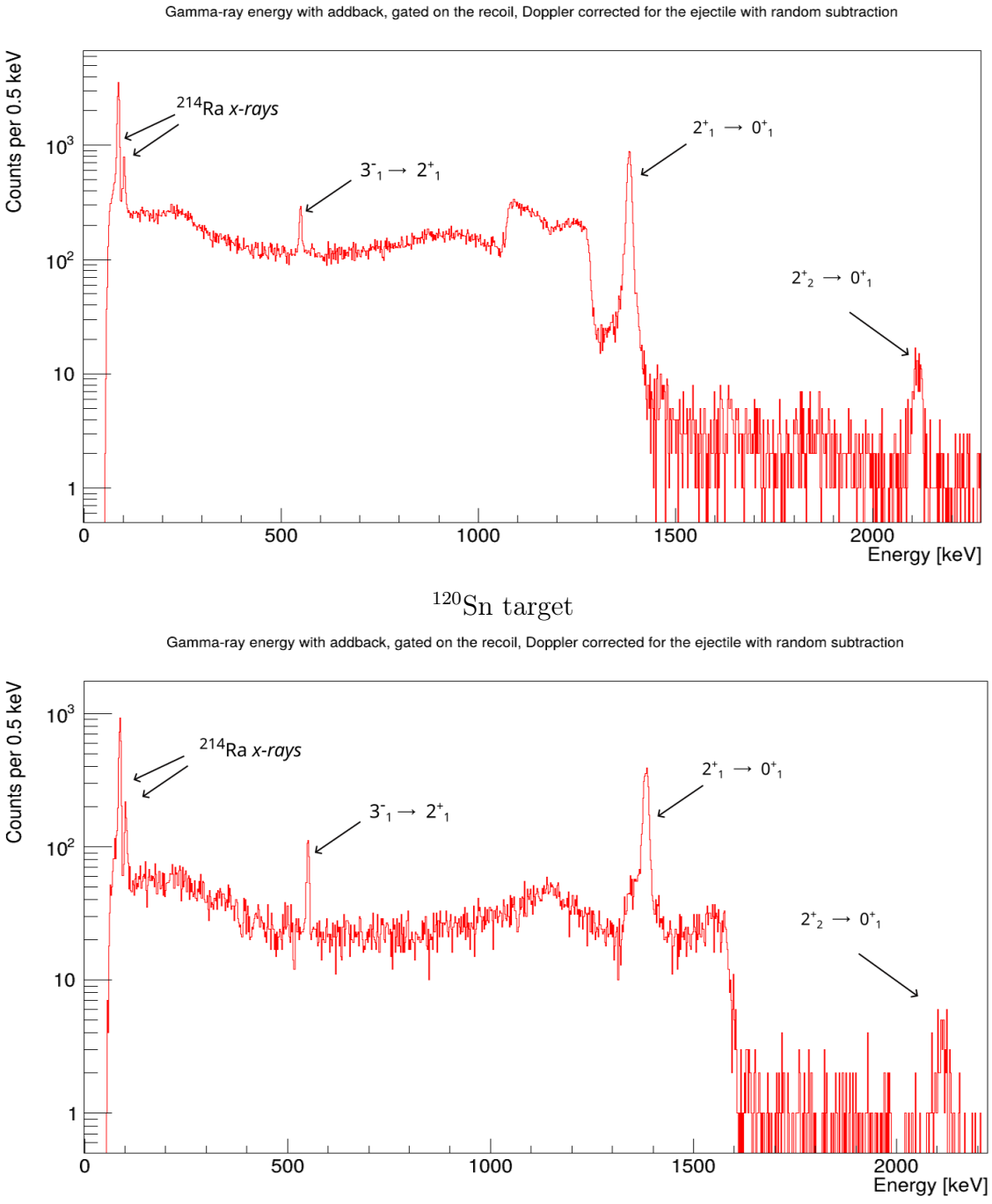

Figure 4.11: Doppler-corrected γ-ray energy spectra obtained in coincidence with scattered particles for (a) the ^{120}Sn target and (b) the ^{58}Ni target. Transitions assigned to Coulomb excitation of ^{214}Ra are labeled.

Figure 4.11 shows the Doppler-corrected γ-ray energy spectra obtained in coincidence with scattered particles for the ^{120}Sn and ^{58}Ni targets. The spectra are summed over all Miniball detectors and include the full statistics after timing and particle-selection conditions. Transitions assigned to excited states in ^{214}Ra populated in the Coulomb-excitation reaction are indicated.

For the ^{120}Sn target, a complication that emerged during the analysis is the unexpectedly large number of X-rays observed in coincidence with the $2_1^+ \rightarrow 0_1^+$ transition. The

working assumption is that a strongly converted 0^+ state is located just above the 2_1^+ level and decays into it, accounting for nearly 5% of the observed population. However, since no γ ray from this state is observed, its excitation energy cannot be determined experimentally. Evidence for this interpretation comes from the γ–γ coincidence matrix: the X-ray lines show clear coincidences with the $2_1^+ \to 0_1^+$ transition, while no such coincidences are observed with the $3_1^- \to 2_1^+$ transition. This demonstrates that the X-ray coincidences are not random.

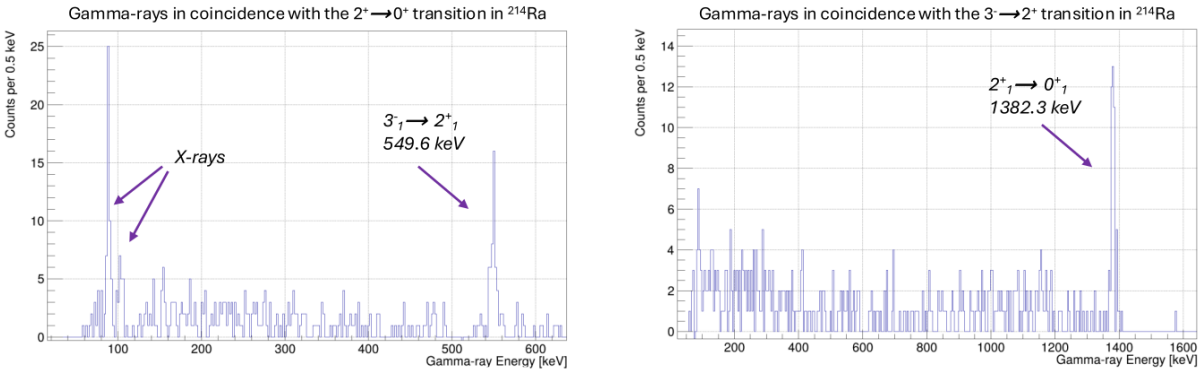

Figure 4.12: Comparison of γ-ray coincidence spectra gated on different transitions in ^{214}Ra. X-ray lines are observed in coincidence with the $2_1^+ \to 0_1^+$ transition, while no corresponding coincidences are present for the $3_1^- \to 2_1^+$ gate.

To quantify the fraction of X-rays associated with the decay of the 0_2^+ state, the yields of the $3_1^- \to 2_1^+$ and $0_2^+ \to 2_1^+$ transitions were compared in coincidence with the $2_1^+ \to 0_1^+$ transition. Since both states feed the 2_1^+ level and do not populate other states, this comparison provides a direct estimate of the relative contribution of atomic X-rays and X-rays originating from the decay of the proposed 0_2^+ state. This introduces a significant ambiguity in the interpretation of the data and limits the extent to which the level scheme can be constrained.

In contrast to the ^{120}Sn data set, no statistically significant X-ray coincidences are observed for the ^{58}Ni target. In particular, no X-ray lines are found in coincidence with the $2_1^+ \to 0_1^+$ transition in the ^{58}Ni data. This behavior is consistent with the interpretation of the X-ray coincidences as originating from the decay of a strongly converted 0_2^+ state. The heavier ^{120}Sn target favors multi-step Coulomb excitation, enhancing the population of such states, whereas the lighter ^{58}Ni target is dominated by single-step excitation.

The population of the 4_1^+ state is found to be very weak in the present data set and is not observed for the ^{58}Ni target. For the ^{120}Sn target, its comparatively long lifetime implies that the decay occurs predominantly after implantation of the beam in the DSSSD, rather than in flight. Evidence for this behavior is provided by the observation of a $4_1^+ \to 2_1^+$ transition in the Doppler-uncorrected γ-ray spectrum. Furthermore, a corresponding $2_1^+ \to 0_1^+$ transition is observed in the uncorrected spectrum, originating from the subsequent decay of the 2_1^+ state populated by the delayed decay of the 4_1^+ level.

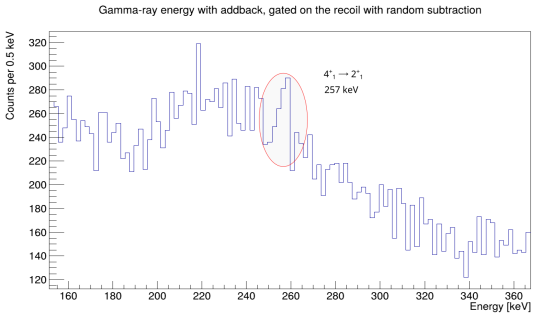

(a) Doppler-uncorrected γ-ray spectrum showing the $4_1^+ \rightarrow 2_1^+$ transition.

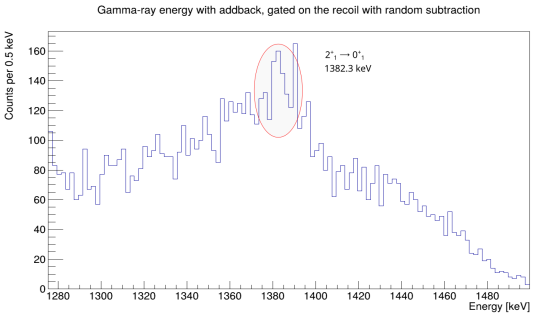

(b) Doppler-uncorrected γ-ray spectrum showing the $2_1^+ \rightarrow 0_1^+$ transition populated by the decay of the 4_1^+ state.

Figure 4.13: Doppler-uncorrected γ-ray spectra illustrating delayed decays following implantation of the beam-like ^{214}Ra ions in the DSSSD. The presence of the $4_1^+ \rightarrow 2_1^+$ transition and the subsequent $2_1^+ \rightarrow 0_1^+$ decay in the uncorrected spectra indicates that the 4_1^+ state decays predominantly after the ions have stopped in the detector.

Experimental yields

The primary objective of the analysis is to determine the relative intensities of the observed γ-ray transitions with the smallest possible uncertainties. The extraction of the transition intensities was carried out using HDTV. In the case of X-rays from nuclear origin, the corresponding yields were derived from γ–γ coincidence spectra. As discussed in the previous section, this was achieved by comparing the coincidence yields of the $3_1^- \rightarrow 2_1^+$ and $0_2^+ \rightarrow 2_1^+$ feeding transitions gated on the $2_1^+ \rightarrow 0_1^+$ transition.

The extracted yields were corrected for the efficiency of the Miniball array and are summarized separately for the ^{120}Sn and ^{58}Ni targets. Only transitions that could be reliably identified under the applied selection conditions are listed.

Table 4.3: Preliminary γ-ray and nuclear X-ray yields for ^{214}Ra obtained with the ^{120}Sn target.

E_i (keV)	J_i^π	E_f (keV)	J_f^π	E_γ (keV)	I_γ	$\pi\lambda$
?	(0_2^+)	1382.3	2_1^+	X-ray	626(150)	–
1382.3	2_1^+	0	0_1^+	1382.3	13334(170)	E2
1639.3	4_1^+	1382.3	2_1^+	257	96(27)	E2
1931.9	3_1^-	1382.3	2_1^+	549.6	802(46)	E1
2114	2_2^+	0	0_1^+	2114	300(40)	E2

Table 4.4: Preliminary γ-ray yields for ^{214}Ra obtained with the ^{58}Ni target. No statistically significant coincidences with X rays were observed for this target, and the population of the 4_1^+ state is not observed in the present data set.

E_i (keV)	J_i^π	E_f (keV)	J_f^π	E_γ (keV)	I_γ	$\pi\lambda$
?	(0_2^+)	1382.3	2_1^+	X-ray	–	–
1382.3	2_1^+	0	0_1^+	1382.3	4712(120)	E2
1639.3	4_1^+	1382.3	2_1^+	257	–	E2
1931.9	3_1^-	1382.3	2_1^+	549.6	301(23)	E1
2114	2_2^+	0	0_1^+	2114	85(17)	E2

Summary and conclusions

A safe Coulomb-excitation experiment on ^{214}Ra was performed at ISOLDE using ^{120}Sn and ^{58}Ni targets, with γ rays detected by the Miniball array and scattered particles recorded in a double-sided silicon strip detector (DSSSD). The motivation of the measurement is to constrain the collectivity of low-lying states near the $N = 126$ shell closure, in particular through the $B(E2; 2_1^+ \rightarrow 0_1^+)$ transition strength.

A major part of the present work was the development of an analysis procedure for extracting Coulomb-excitation yields with minimized uncertainty. The DSSSD calibration required dedicated treatment due to gain instabilities and radiation-damage effects. Kinematic simulations and p–n correlation method were used to obtain a consistent energy response across detector quadrants.

The Doppler-corrected γ-ray spectra show clear population of the 2_1^+, 3_1^- and 2_2^+ states in ^{214}Ra for both targets. For the ^{120}Sn target, an additional and unexpected feature was observed: pronounced X-ray lines are in coincidence with the $2_1^+ \rightarrow 0_1^+$ transition. The working interpretation is that a strongly converted 0^+ state lies above the 2_1^+ level and decays predominantly by internal conversion, producing X rays that appear in coincidence with the $2_1^+ \rightarrow 0_1^+$ transition. This introduces an ambiguity in the feeding of the 2_1^+ state and limits how tightly the level scheme can be constrained from the present data alone. No statistically significant X-ray coincidences were observed for the ^{58}Ni target, consistent with reduced multi-step excitation and feeding for the lighter target.

The extracted preliminary yields for both targets were summarized in Tables 4.3 and 4.4. These yields form the experimental input for a subsequent Coulomb-excitation analysis aimed at determining electromagnetic matrix elements, in particular the $E2$ matrix element of the $2_1^+ \rightarrow 0_1^+$ transition.

The next step of the analysis is a coupled-channel Coulomb-excitation fit using the GOSIA [20] code. GOSIA calculates excitation cross sections for a given set of electric and magnetic matrix elements and compares the resulting γ-ray yields to the experimentally determined values in a least-squares procedure. By simultaneously treating transitions observed for both targets, this approach enables the extraction of reduced transition probabilities and quadrupole matrix elements consistent with the measured data.

In conclusion, the present work establishes the analysis procedure and provides the current best set of experimental yields for low-lying transitions in ^{214}Ra from the HIE-ISOLDE Coulomb-excitation experiment. With the final yield set and a consistent treatment of feeding, the forthcoming GOSIA analysis is expected to deliver a meaningful constraint on quadrupole collectivity at $N = 126$ and to provide a benchmark for shell-model-based descriptions in this region.

Bibliography

[1] I. Talmi, "Simple Models of Complex Nuclei," Nucl. Phys. A **172**, 1 (1971).

[2] N. Warr *et al.*, "The Miniball spectrometer," Eur. Phys. J. A **49**, 40 (2013).

[3] R. F. Casten, *Nuclear Structure from a Simple Perspective*, Oxford University Press, Oxford (1990).

[4] D. Kocheva *et al.*, Phys. Rev. C **104**, 024311 (2021).

[5] B. A. Brown, Phys. Rev. Lett. **85**, 5300 (2000).

[6] E. Grodner *et al.*, "Reduced collectivity near the $N = 126$ shell closure," Phys. Rev. Lett. **109**, 072501 (2012).

[7] T. Möller, *Aspects of Nuclear Collectivity Studied in Projectile Coulomb Excitation Experiments*, Ph.D. thesis, Technische Universität Darmstadt (2014).

[8] D. Cline, Annu. Rev. Nucl. Part. Sci. **36**, 683 (1986).

[9] J. F. Ziegler and J. P. Biersack, Nucl. Instrum. Methods Phys. Res. B **268**, 1818 (2010), `http://www.srim.org`.

[10] M. Borge and Y. Kadi, "ISOLDE at CERN," Nucl. Phys. News **26**(4), 6–13 (2016), doi:10.1080/10619127.2016.1249214.

[11] RILIS Collaboration, *Resonance Ionization Laser Ion Source (RILIS)*, CERN, `https://rilis-web.web.cern.ch/training`, accessed 2024.

[12] A. Müller *et al.*, *The REX-EBIS Charge Breeder*, CERN Report OPEN-2000-320 (2000), `https://cds.cern.ch/record/478399`.

[13] HIE-ISOLDE Collaboration, *The HIE-ISOLDE Project*, CERN, `https://hie-isolde-project.web.cern.ch/hie-isolde-project/`, accessed 2024.

[14] F. Ames *et al.*, "REXTRAP: A Penning trap for the accumulation and charge breeding of radioactive ions," Nucl. Instrum. Methods Phys. Res. A **538**, 17–48 (2005).

[15] L. P. Gaffney, *Kinsim – DSSSD kinematic calculations*, GitHub repository, `https://github.com/lpgafff/kinsim`, original release 2021, regularly updated (accessed 2024).

[16] G. F. Knoll, *Radiation Detection and Measurement*, 4th ed., Wiley, New York (2010).

[17] A. Görgen *et al.*, "Particle–γ coincidence techniques with double-sided silicon strip detectors," Nucl. Instrum. Methods Phys. Res. A **723**, 53–63 (2013).

[18] Miniball Collaboration, *MiniballCoulexSort: Data sorting and analysis software for Coulomb-excitation experiments*, GitHub repository, `https://github.com/Miniball/MiniballCoulexSort`, (accessed 2024).

[19] J. Mayer, *HDTV – Nuclear Spectrum Analysis Software*, GitHub repository, `https://github.com/janmayer/hdtv`, latest update 26 Oct 2024 (accessed 2024).

[20] D. Cline, T. Czosnyka, A. B. Hayes, P. Napiorkowski, N. Warr and C. Y. Wu, *GOSIA: User Manual for Simulation and Analysis of Coulomb Excitation Experiments*, University of Rochester (2012).